Materials Advances

ROYAL SOCIETY OF CHEMISTRY

PAPER

View Article Online
View Journal | View Issue

Cite this: *Mater. Adv.*, 2025, 6, 3114

Promising wound healing activity of *Saussurea costus* loaded PCL–gelatin nanofibers†

Jude Majed Lababidi,[a] Mostafa Fytory,[ab] Abd Elrahman Abouzid,[c] Jihad El-Qassas,[cd] Aya T. Gad,[e] Osama M. Ahmed,[e] Nagwa El-Badri*[c] and Hassan Mohamed El-Said Azzazy*[a]

Wound healing is a complex process, including inflammation, tissue formation, and remodeling. *Saussurea costus* (Sc) is reported to possess antimicrobial and anti-inflammatory activities. In this study, we manufactured polycaprolactone–gelatin nanofibers loaded with 6% Sc extract (PCL–GL-6% Sc) for wound healing applications. Comprehensive characterization confirmed the structural integrity and functionality of the prepared nanofibers. SEM results showed an increase in diameter of PCL–GL upon encapsulation of Sc. FTIR and XRD verified chemical bonding and crystallinity of the nanofibers, respectively. TGA demonstrated thermal stability, while tensile strength testing confirmed durability, and both parameters are critical for wound dressing applications. The Sc release profile showed controlled bioactive release, which supports sustained healing effects. Lastly, contact angle measurements indicated hydrophilicity, supporting cellular adhesion, which is necessary for wound recovery. Antimicrobial assessments showed significant activities of PCL–GL-6% Sc nanofibers against *Pseudomonas aeruginosa*, *Staphylococcus aureus*, and *Escherichia coli*, with a log reduction of around 7 in the PCL–GL-6% Sc group. Cytotoxicity tests on human skin fibroblasts revealed no significant difference between PCL–GL-6% Sc treated cells *vs.* untreated cells. *In vivo* studies in albino rats showed enhanced epithelial regeneration and collagen deposition, with significant downregulation of interleukin-6 (IL-6) ($p \leq 0.05$) and upregulation of B-cell lymphoma protein 2-associated X (BAX) ($p \leq 0.0001$) and matrix metalloproteinase-3 (MMP-3) ($p \leq 0.01$). Immunohistochemistry supported these findings with moderate expression of vascular endothelial growth factor (VEGF) and transforming growth factor beta-1 (TGF-β1), alongside high BAX expression. In conclusion, PCL–GL-Sc 6% Sc holds potential as an effective dressing for wound healing applications.

Received 4th December 2024,
Accepted 23rd March 2025

DOI: 10.1039/d4ma01196a

rsc.li/materials-advances

1. Introduction

Wound healing is a complex biological process which aims to recover the functional and structural integrity of injured skin. Upon skin injury, hemostasis is activated to stop bleeding by the formation of blood clots. This is then followed by an inflammatory response with the mobilization of white blood cells to the site of injury to combat the invading pathogens and prevent microbial infections. Subsequently, the proliferation phase takes over which involves new tissue formation, collagen synthesis, and angiogenesis.[1] While the body has a remarkable ability to heal itself, several challenges could disturb normal wound healing. Microbial infection is one of the most significant concerns because it could delay healing and increase tissue damage, leading to systemic problems including sepsis in some severe cases.[2] Guan *et al.* reported a significant prevalence of microbial infections (63.9%) in skin wounds in their study.[3] Furthermore, the wound environment, including moisture balance, can significantly impact the healing process.[4] Identifying the specific bacteria in the wound microbiota is suggested to help tailor treatment and successful wound healing.[5] Common bacteria causing wound infections include *Escherichia coli* (*E. coli*), *Pseudomonas aeruginosa* (*P. aeruginosa*), and *Staphylococcus aureus* (*S. aureus*).[2]

Wound dressings serve as the frontline intervention in wound care, and are applied immediately after injury because they provide a physical barrier to the wound and reduce the risk of infection.[6] Additionally, antibiotics play a crucial role in

[a] *Department of Chemistry, School of Sciences & Engineering, The American University in Cairo, AUC Avenue, P.O. Box 74, New Cairo 11835, Egypt. E-mail: hazzazy@aucegypt.edu; Tel: 00 202 2615 2559*
[b] *Material Science and Nanotechnology Department, Faculty of Postgraduate Studies for Advanced Sciences (PSAS), Beni-Suef University, 62511 Beni-Suef, Egypt*
[c] *Center of Excellence for Stem Cells and Regenerative Medicine, Zewail City of Science and Technology, Giza, 12578, Egypt. E-mail: nelbadri@zewailcity.edu.eg*
[d] *Zoology Department, Faculty of Science, Zagazig University, 4541519 Zagazig, Egypt*
[e] *Physiology Division, Zoology Department, Faculty of Science, Beni-Suef University, Beni-Suef 62521, Egypt*

† Electronic supplementary information (ESI) available. See DOI: https://doi.org/10.1039/d4ma01196a

combating bacteria that attempt to invade wounds. Given the rise of bacterial resistance to antibiotics, alternative strategies have been developed for managing wound infections, including the use of antimicrobial agents derived from natural sources to promote wound healing while minimizing the risk of antimicrobial resistance.[7]

Natural products such as *Curcuma longa L* play an important role in wound healing, offering a variety of therapeutic benefits. Extracts of *Blumea balsamifera* and Aloe vera have been reported to stimulate collagen synthesis, essential for wound closure. Additionally, herbal extracts of *Cordia verbenacea DC* and honey promote angiogenesis and increase the expression of growth factors. Natural extracts that possess anti-inflammatory and antioxidant properties help modulate inflammatory responses and oxidative stress.[8,9] Moreover, many herbal extracts, such as *Matricaria chamomilla*, *Astragalus membranaceus*, *Cinnamomum cassia*, and *Blumea balsamifera* exhibit antibacterial properties, crucial for preventing infections in wounds. It is of note that around 80% of the population worldwide primarily relies on plant-derived substances to treat various health conditions.[10] The Indian Himalayan region represents a remarkable repository of botanical diversity.[11] One of the important species in this region is *Saussurea costus* (Sc), a member of the Asteraceae family, which is known for its powerful healing properties and has been central to Chinese and Ayurvedic medicine for many years.[12] The examination of the phytochemical composition of Sc unveiled diverse types of bioactive elements such as steroids, flavonoids, lignans, monoterpenes, triterpenes, and glycosides.[13] For instance, the ethanolic extract of Sc is reported to have powerful natural antioxidant,[13–15] anti-urolithiasis,[15] anti-microbial,[16–20] anti-viral,[16,18] anti-inflammatory,[18] nephroprotective,[21] anti-cancer,[19,22] and anti-obesity[23] activities.

Electrospun nanofibers exhibit unique advantages making them suitable for wound healing applications.[24] Their structure closely resembles the extracellular matrix (ECM) of natural tissue, providing a supportive environment for wound healing. With a high surface area to volume ratio, nanofibers maintain a moist gas environment through promoting gas exchange.[25] Additionally, the materials commonly used in electrospinning are biocompatible and biodegradable polymers that serve as carriers for bioactive natural molecules, enabling sustained and direct delivery of loaded drugs to the wound site.[26] Poly-ε-caprolactone (PCL), a synthetic biodegradable polymer, and gelatin (GL) have emerged as prominent choices among the diverse selection of natural and synthetic biodegradable polymers for wound dressing applications.[27] Exploration of these materials has highlighted their resemblance to the ECM. Additionally, PCL offers excellent mechanical strength and biocompatibility. Its slow degradation rate ensures prolonged support and controlled drug release, and thus enhanced therapeutic outcomes.[28] On the other hand, GL, derived from collagen, promotes cell attachment and tissue regeneration.[29] When combined with natural antimicrobial products, PCL–GL composite fibers exhibit a synergistic wound healing effect, which promotes skin tissue repair and enables controlled release of the loaded antimicrobial agents. The synergy of these materials has proven to be effective in many studies. For example, PCL–GL nanofibrous mats loaded with a bark extract of *Pinus radiata* showed promising activity of these nanofibers, suggesting their efficacy as dressings for wound healing.[30] Likewise, another group loaded *Calendula officinalis* extract in electrospun PCL–GL nanofibers, which showed suitable attributes for application as wound dressings.[31]

This study aimed to develop PCL–GL nanofibers incorporating varying concentrations of Sc extract, intended as an antimicrobial wound dressing. Morphological characteristics, diameter, physical properties, thermal stability, and wettability, as well as tensile properties of the electrospun nanofibers were elucidated. Additionally, the release of Sc extract from the PCL–GL nanofibers and their kinetics was investigated together with their cytotoxicity profiles to ensure biocompatibility. *In vitro* assessments of the antimicrobial efficacy, as well as *in vivo* assessment of wound healing efficacy in a rat model were conducted. Furthermore, immunostaining and molecular studies to shed light on the relevant wound healing mechanisms promoted by the Sc extract-loaded PCL–GL nanofibers were performed.

2. Material and methods

2.1. Materials

Cell culture. Dulbecco's modified Eagle medium (DMEM) was utilized to culture human skin fibroblast (HSF) cell line (VACCERA, Cairo, Egypt) with fetal bovine serum (FBS) adjusted at 10%.

Bacterial strains. In this study, three standard strains of bacteria, *S. aureus*, *P. aeruginosa*, and *E. coli* (ATCC numbers 25923, 27853, and 25922, respectively) were used (Nawah Scientific Inc. Cairo, Egypt). Bacteria were allowed to grow in broth and then incubated overnight at 37 °C.

Chemicals. PCL (MW: 80 000 g mol^{-1}) was obtained from Spectrum Chemical Mfg. Corp. (Gardena, USA). Formic acid and acetic acid were acquired from Chem-Lab NV (Belgium), and absolute ethanol from CARLO ERBA Reagents (Val de Reuil, France). Phosphate buffered saline (PBS) tablets were obtained from Genetix Biotech Asia Pvt. Ltd (India), and 1,1-diphenyl-2-picrylhydrazyl (DPPH) was purchased from Sigma-Aldrich (Germany). DMEM was acquired from Gibco (Thermo-scientific, Regensburg, Germany), while streptomycin–penicillin mix was obtained from Lonza (Basel, Switzerland). AlamarBlue was sourced from Merck (KGaA, Darmstadt, Germany). Sc roots used in this study were obtained from Rajab-Alattar (Cairo, Egypt). All chemicals were of ultra-pure grade and commercially available. The following kits were acquired: HERA PLUS SYBR® Green Kit (Willowfort, UK), cDNA Synthesis Kit (Thermo Fisher, Carlsbad, CA, USA), VEGF kit (GServicebio®, China), TGF-β1 kit (ABClonal, Germany), BAX kit (ABClonal, Germany), and DAB (Thermo Scientific, USA).

2.2. *Saussurea costus* (Sc) extract preparation

Plant roots were crushed into a fine powder using an electric mixer grinder. The extraction followed the maceration method, in which the fine powder was mixed separately with ethanol.

In a tightly sealed dark container, these mixtures were left in a shaking incubator at 37 °C and a 100 rpm shaking speed for 3 days. Following incubation, the mixture was filtered using Whatman filter paper No. 1. The obtained filtrates underwent solvent evaporation using a rotary evaporator to obtain the extract, which was stored at 4 °C until needed.[32]

2.3. Characterization of the Sc extract

2.3.1. Gas chromatography-mass spectrometry (GC-MS). The chemical components in the ethanolic extract were identified using an Agilent Technologies GC-MS/7890B coupled with a 5977B mass spectrometer detector based on a prior report following the same parameters.[33]

2.4. Fabrication of free and Sc extract loaded-PCL–GL (PCL–GL-Sc) nanofibers

Several experiments were undertaken to determine the ideal quantities of PCL and GL, as well as the most suitable solvent or solvent mixture, to produce nanofibers characterized by a smooth, well-defined shape with no beads. The use of acetic acid alone as a solvent did not yield optimal results. However, incorporating 10% formic acid with acetic acid as the solvent for PCL–GL resulted in the formation of bead-free nanofibers.[34] Fabrication of the nanofibers began with the dissolution of GL (1.5%, w/v) and PCL (13.5%, w/v) in acetic acid : formic acid (9 : 1), and the mixture was left overnight on a stirrer at room temperature, maintaining a total polymer concentration of 15% (w/v). Different concentrations of Sc extract (2%, 4%, and 6%, w/v) were added separately to the PCL–GL solution based on the results of the initial antimicrobial tests. The polymer solution was loaded into a 5 mL glass syringe (SK-500II, Shenzhen Mindray Scientific Co., Ltd, China) for electrospinning at a rate of 0.6 mL h^{-1}. An electrospinning voltage in the range of (20.5–24 kV) was applied between the aluminum collector and the needle. The collected nanofibers were left to dry overnight.

2.5. Characterization of the nanofibers

2.5.1. Morphology, size, and fast Fourier transform (FFT) analysis for nanofiber alignment. A LEO Supra 55 field emission scanning electron microscope (FE-SEM) manufactured by Zeiss (Oberkochen, Baden-Württemberg, Germany) was used to assess the morphology and diameter of the formed nanofibers (PCL–GL-2% Sc, PCL–GL-4% Sc, and PCL–GL-6% Sc). Then, the average diameter of the nanofibers (measured in triplicates) was determined using ImageJ software (NIH, Bethesda, MD, USA).

To perform FFT analysis on free and loaded nanofibers, ImageJ software was utilized where SEM images exhibited dimensions of 2048 × 2048 pixels (8-bit depth) in grayscale format. The resulting FFT spectrum displayed spatial frequency components, with the central region representing low frequencies (large structures) and the periphery representing high frequencies (fine structures). Isotropic patterns appeared as uniform circular features, while streaks or directional features indicated alignment.[35] The alignment of PCL–GL, PCL–GL-2% Sc, PCL–GL-4% Sc, and PCL–GL-6% Sc nanofibers was analyzed with the directionality plugin in ImageJ/Fiji. The spatial arrangement of features in the entire SEM images was analyzed and processed using fast Fourier transform (FFT), converting the image from the spatial domain to the frequency domain (structural orientation is represented in terms of directional patterns). A histogram of angles (0°–180°) *vs.* normalized frequencies was generated. Flat regions in the histogram represent isotropic random distributions, while sharp peaks represent dominant orientation.[35,36]

2.5.2. Fourier-transform infrared spectroscopy (FTIR). The analysis of the functional groups in Sc, free PCL–GL, and PCL–GL-Sc was conducted using FTIR (Nicolet 380 FT-IR, Thermo-Scientific, Madison, USA). For the Sc extract, the procedure involved applying a small amount of the extract onto a KBr, positioning it directly in front of the infrared beam. For the nanofiber cuts, KBr was mixed with them. Next, these mixtures were compressed into small discs using a 15-ton manual press machine. Subsequently, the resulting discs were subjected to an infrared beam for IR analysis.[37] The spectrum examination covered wavenumbers ranging from 400 to 4000 cm^{-1}. This approach allowed for a detailed investigation of the molecular vibrations and functional groups present in the nanofibers to identify their chemical composition.

2.5.3. X-ray diffraction (XRD) of the nanofibers. To analyze the diffraction pattern produced when X-rays interact with the produced nanofibers, a model 4040 X-ray diffractometer (Bruker, USA) was utilized. The XRD patterns provided insights into the crystalline structures in both free and loaded nanofibers. Cu Kα radiation with a wavelength of 0.15406 Å was employed and scanning done over a range of 2θ from 5° to 80°.

2.5.4. Thermal stability. A thermogravimetric analyzer (TGA-Q50, TA Instruments, USA) was used to analyze the thermal properties. Samples weighing 1 mg were heated from (25 °C to 800 °C, 10 °C $minute^{-1}$) under a nitrogen flow. The sample's weight loss in response to the rising temperature was recorded.

2.5.5. Tensile strength. A TS1500 1500N testing machine (TSL solutions, Acutance Scientific©, Tunbridge Wells, Kent, UK) was utilized to investigate the tensile strength of PCL–GL, PCL–GL-2% Sc, PCL–GL-4% Sc, and PCL–GL-6% Sc. Triplicates of randomly selected samples (2 mm × 10 mm) were subjected to a cross-head speed test at 16.86 mm min^{-1}. Young's modulus, ultimate strength, yield strength, and elongation at break were determined for all loaded and free nanofibers in triplicate.

2.5.6. *In vitro* drug release profile. The quantification of Sc extract release from the nanofiber involved placing a predetermined weight of the nanofiber (PCL–GL-2% Sc, PCL–GL-4% Sc, and PCL–GL-6% Sc) with an average surface area of 1 cm^2 equivalent to approximately (10 mg) into a Falcon tube. Subsequently, the samples were incubated in PBS solution (pH 7.4) at 37 °C in a shaking incubator. At predetermined time intervals, an accurate volume of PBS (3 mL) was removed and compensated with fresh PBS at the same volume. The measurement of Sc release was accomplished by measuring absorbance at 275 nm using a Cary 3500 UV-Vis Engine spectrophotometer (Agilent Technologies Australia (M) Pty Ltd, Mulgrave, Australia), utilizing a previously established calibration curve of Sc. This method allowed for the systematic tracking of

Sc release over time. Following this, the cumulative percentage of Sc released was determined utilizing eqn (1).

$$\text{Cumulative release } (\%) = \frac{\text{amount released}}{\text{initial amount}} \times 100 \quad (1)$$

2.5.7. Release kinetics of Sc extract from the nanofibers. Understanding the kinetics and the mechanisms of release of Sc extract is essential for evaluating the nanofiber system.[38] In this study, various kinetic models were employed to investigate the cumulative release percent of Sc extract from loaded nanofibers over 12 hours. The data was subjected to kinetic models described by eqn (2)–(6) to elucidate the mechanism of the release kinetics in the initial burst release of Sc extract.[39–41]

Zero-order model

$$[A]_t = [A]_0 - k_0 t \quad (2)$$

First-order model

$$\log A_t = \log A_0 - \left(\frac{k_1}{2.303}\right) t \quad (3)$$

Higuchi model

$$A_t = k_{HC}(t^{1/2}) \quad (4)$$

Hixson–Crowell model

$$\sqrt[3]{A_0} - \sqrt[3]{A_t} = k_H t \quad (5)$$

Korsmeyer–Peppas model

$$A_t/A_\infty = k_{kp} t n \quad (6)$$

A_t: concentration of the extract released at time t; A_0: initial concentration of the extract; A_t/A_∞: fraction released at time t; n: release exponent; k_0, k_1, k_H, k_{HC}, and k_{kp}: release rate constants of zero-order, first-order, Higuchi, Hixson–Crowell, and Korsmeyer–Peppas kinetic models, respectively.

2.5.8. Contact angle of the nanofibers. The assessment of the surface hydrophilicity in the nanofibers (PCL–GL-2% Sc, PCL–GL-4% Sc, and PCL–GL-6% Sc) involved the determination of the contact angle formed between a droplet of water and the nanofiber. For this purpose, a 1.5 μL water droplet was deposited onto the surface using a micro syringe, and a static image was captured using the Drop Shape Analyzer (DSA25S, KRUSS, Germany). Three measurements were taken at different positions.

2.6. *In vitro* biological activity

2.6.1. Antimicrobial assessment of Sc extract and nanofibers. The minimum inhibitory concentration (MIC) of Sc ethanolic extract was determined utilizing the microdilution method. First, initial stock solutions of Sc were prepared, following 10-fold serial dilutions. Bacterial inoculums of *E. coli*, *P. aeruginosa*, and *S. aureus* were adjusted to 0.5 McFarland standard and then diluted to a concentration of 1.0×10^6 CFU mL^{-1}. Subsequently, 10 μL of the inoculum was added to each well. After incubation for 24 h, 20 μL of freshly prepared AlamarBlue (resazurin) were added to the 96-well plate and reincubated for another 3 h. The change of color from blue to pink indicated bacterial growth. The minimum concentration of Sc extract that maintained the blue color (no color change) was considered the MIC.[42] This MIC value was then incorporated into the PCL–GL nanofiber matrix as the starting concentration for further studies, ensuring effective antibacterial properties in the nanofiber-based delivery system.

For antimicrobial assessment of PCL–GL and PCL–GL- (2, 4, and 6%) Sc nanofibers, the ISO 20743:2021 protocol was followed. Triplicates of nanofibers were cut with an average surface area of 1 cm^2 equivalent to approximately 10 mg, sterilized under UV light, and placed in 50 mL Falcon tubes. Following this, the bacterial cultures of *P. aeruginosa*, *S. aureus*, and *E. coli* were adjusted to 0.5 McFarland standard using an Omega FLUOstar microplate reader. Further dilutions to reach log 5 per mL were made, and 50 μL of the inoculum was applied to the fabrics under sterile conditions for 24 h incubation. Afterward, the nanofibers were washed with 10 mL PBS, and then 100 μL of them was spread on sterile nutrient agar. The agar plates were incubated overnight for colony counting. For both, free PCL–GL nanofibers and control samples, dilutions were performed to facilitate accurate colony counting.[43]

2.6.2. Free-radical scavenging efficiency of the nanofibers. For antioxidant activity assessment of PCL–GL-2% Sc, PCL–GL-4% Sc, and PCL–GL-6% Sc, DPPH was utilized in which 5 mg of the nanofibers were placed in a 3 mL methanolic solution of DPPH (0.12 mM) and left to incubate in darkness for 30 min. Triplicates (200 μL) of the mixtures were measured at 517 nm using a FLUOstar microplate reader (BMG Labtech, Germany). The DPPH scavenging activity was determined using the following (eqn (7))

$$\%\ \text{DPPH scavenging} = \left[\frac{A_b - A_s}{A_b}\right] \times 100 \quad (7)$$

A_b: absorbance of DPPH methanolic solution; A_s: absorbance of the sample mixture.

2.6.3. Biocompatibility assessment with MTT assay. The MTT assay was done to assess the biocompatibility of the nanofiber materials to ensure that they do not exert adverse effects that may hinder the healing process.[44] Human skin fibroblast (HSF) cells were seeded at a density of 3×10^3 cells per well in DMEM (10% FBS), in 96-well plates, and left for 24 h to allow cell attachment. Then, 100 μg of PCL–GL-6% Sc nanofibers were cut using sterile scissors and sterilized under UV light for 20 min. PCL–GL-6% Sc nanofibers were then carefully added to the inner walls of the wells and left overnight to assess the effect of the nanofiber on the HSF cells. Next, an MTT assay was performed, in which 40 μL of fresh medium and 50 μL of MTT (1 mg mL^{-1} in PBS) were added to each well and the plates were incubated at 37 °C for 4 h. Afterward, the MTT solution was replaced with 250 μL of DMSO. At 570 nm, optical density (OD) was measured using a SPECTROstar Omega microplate reader (BMG LABTECH, Germany). Five replicates of each sample were prepared, along with a negative control (untreated cells).

2.7. *In vivo* wound healing

2.7.1. Surgical process. All the procedures were conducted according to the guidelines outlined by the National Institutes

of Health (NIH) and the Committee for Control and Supervision of Experiments on Animals (CPCSEA). The Animal Ethics Committee of the Zoology Department in the College of Science at Beni-Suef University approved the study protocol with ethical approval number (024-008). Twenty-one male albino rats (Vacsera, Cairo, Egypt), averaging 131.31 ± 14.97 g in weight, were housed under controlled conditions with access to water and food.

For the experimental setup, rats were anesthetized with xylazine and ketamine at 7 mg kg^{-1} and 60 mg kg^{-1}, respectively. Subsequently, two wounds were created on the left and right sides of the shaved dorsum of each rat using a surgical sterile punch, each measuring 1.5 cm in diameter. The wound sizes on days 7 and 14 were determined. Wound closure was measured by calculating the reduction in wound area as compared to its initial size over time. Additionally, the weight change of rats was tracked by comparing their starting weight to their weight at the end of the study.

The rats were divided into 3 groups: normal group without wounds, negative control group injured but not treated, and treatment group using PCL–GL-6% Sc nanofibers. To minimize chance bias, each experimental group received treatments in different sequences across the dorsal surfaces of seven rats, each presenting with two wounds. After 14 days, the rats were euthanized using diethyl ether and sacrificed. Tissue and blood samples, for further analysis, were obtained.

Blood samples from the carotid artery were allowed to coagulate followed by centrifugation to separate the serum. The clear serum was subsequently stored at −20 °C until further analysis. Neutral buffered formalin was used to fix wound tissues for blocking, sectioning, and staining.

2.7.2. White blood cell count determination. Blood samples were collected from the carotid artery into EDTA tubes to prevent clotting. Samples were analyzed to determine the total lymphocyte count, along with the specific counts of lymphocytes, segmented neutrophils, monocytes, and eosinophils, using a Giemsa stain for staining blood smears and a hematology analyzer.

2.7.3. RNA extraction, cDNA synthesis, and quantitative real time-polymerase chain reaction (qRT-PCR). Skin tissue samples of both the negative control and PCL–GL-6% Sc treated groups were collected to perform RNA extraction. Initially, liquid nitrogen was added to the samples to facilitate the grinding process, which were then stored at −80 °C in 1 mL of Trizol (Invitrogen, Carlsbad, California, USA). RNA extraction was performed according to the protocol of the manufacturer. The concentration of RNA in the final eluates was measured using a SPECTROstar Nano spectrophotometer (BMG LABTECH, Offenburg, Germany). The synthesis of cDNA was performed using the RevertAid First Strand cDNA Synthesis Kit (Thermo Fisher, Carlsbad, CA, USA). qRT-PCR analysis was carried out in triplicate for each cDNA sample using the HERA PLUS SYBR® Green Kit (Willowfort, UK) according to the manufacturer's guidelines. Gene expression levels were quantified using the $2^{\Delta\Delta CT}$ method, with β-actin serving as the normalization control. Each experiment was repeated twice, and all reactions were conducted in triplicate.[45] The sequences of the used primers were supplied by Invitrogen (Thermo Fisher Scientific, Carlsbad, CA, USA), and are indicated in Table 1.

Table 1 RT-qPCR primers (Invitrogen, Carlsbad, CA, USA)

Gene (protein)	Primer	Sequence (5′ to 3′)
β-actin	Forward	CACCATTGGCAATGAGCGGTTC
	Reverse	AGGTCTTTGCGGATGTCCACGT
Bax	Forward	CAAACTGGTGCTCAAGGCCC
	Reverse	GAGACAGGGACATCAGTCGC
P53	Forward	GGAAGAGAATCTCCGCAAGAA
	Reverse	AGCTCTCGGAACATCTCGAAG
Bcl-2	Forward	GGATAACGGAGGCTGGGATG
	Reverse	TGACTTCACTTGTGGCCCAG
MMP2	Forward	ACTGCCTTCGATACACCGGG
	Reverse	TATTCTTGGGCACCGGGAGG
MMP3	Forward	CACTCACAGACCTGACTCGGTT
	Reverse	AAGCAGGATCACAGTTGGCTGG
MMP13	Forward	TTCGGCTTAGAGGTGACTGGC
	Reverse	TTCACCCACATCAGGAACCCC
TNF-α	Forward	TCTTCTCGAACCCCGAGTGA
	Reverse	CCTCTGATGGCACCACCAG
IL-1	Forward	CGCCAATGACTCAGAGGAAG
	Reverse	AGGGCGTCATTCAGGATCAA
IL-6	Forward	GTAGCCGCCCCACACAGACAGCC
	Reverse	GCCATCTTTGGAAGGTTC
IL-12	Forward	TGGAGTGCCAGGAGGACAGT
	Reverse	TCTTGGGTGGGTCAGGTTTG

2.7.4. Histological and immunohistochemical analyses. Tissue samples from normal (uninjured), negative control (injured, untreated), and PCL–GL-6% Sc-treated groups, were processed for histological analysis. Sections were dehydrated, embedded in paraffin, cut into 4–5 μm slices, and stained with hematoxylin & eosin (H&E) and Masson's trichrome for microscopic examination. For immunohistochemistry (IHC), citrate buffer (pH 6.0) was utilized for antigen retrieval to expose the epitopes. Following this, sections were treated to block non-specific binding sites and then incubated at 4 °C with primary antibodies against VEGF, TGF-β1, or BAX. Afterward, sections were treated with horseradish peroxidase-conjugated secondary antibody, developed using DAB substrate to yield a brown stain, and counterstained with hematoxylin. The stained sections were examined under a light microscope (Leica Microsystems, Wetzlar, Germany), with control sections included to verify the specificity of the staining.

2.8. Statistical analysis

Each formulation was replicated three times, and the results along with the data were reported as the mean ± standard deviation (SD). Comparisons were conducted using one-way ANOVA followed by Tukey's multiple comparison test. The significance was considered at 4 levels as follows: $p \leq 0.05$, $p \leq 0.01$, $p \leq 0.001$, and $p \leq 0.0001$.

3. Results and discussion

3.1. GC-MS of the ethanolic extract

A comprehensive GC-MS analysis of ethanolic extract identified a total of 43 chemical compounds. The top most abundant

compounds were eremanthine (63.13%), followed by dehydrosaussurea lactone (11.61%), dihydrodehydrocostus lactone (5.49%), octadecatrien-1-ol (5.22%), 5-hydroxy-4-methyl 6-hepten-3-one (2.84%), β-costol (1.87%), and costunlide (0.337%). This study highlighted the presence of compounds categorized as sesquiterpenes, oxygenated sesquiterpenes, lactones, and fatty acid derivatives. These results are consistent with earlier published reports, providing validation for the known properties and composition of Sc root extract.[46,47] The gas chromatogram and the compounds present in the ethanolic root extract of Sc with the corresponding percentage are shown in the ESI† (Fig. S1 and Table S1), respectively.

3.2. Characterization of the nanofibers

3.2.1. Morphology, size, and FFT analysis for nanofiber alignment. Several trials were conducted to optimize the amounts of both PCL and GL, as well as to identify the most suitable solvent system for producing nanofibers with smooth, well-defined shapes and consistent diameters. Initial experiments using only acetic acid as the solvent did not yield the best results, with the nanofibers lacking the desired uniformity. However, the addition of 10% formic acid to the acetic acid solvent significantly improved the outcome, resulting in PCL–GL nanofibers that were smooth and free of beads. This improvement could be attributed to the higher dielectric constant of formic acid. The permittivity (dielectric constant) of a solvent is a critical factor in nanofiber formation, as a higher dielectric constant generally facilitates better nanofiber formation through increasing the charge density of the polymer solution, enhancing the electrostatic repulsive forces and increasing the mobility of ions to maintain a stable and continuous jet formation.[48] Acetic acid has a dielectric constant that is ten times lower than that of formic acid.[49] Furthermore, it is worth mentioning that formic acid could degrade GL. However, the utilization of acetic acid in a high percentage (90%) slows down the GL degradation.[50] The morphological characteristics of the PCL–GL, PCL–GL-2% Sc, PCL–GL-4% Sc, and PCL–GL-6% Sc nanofibers were examined using FE-SEM. The size of the formed nanofibers was measured by Image J software. Free PCL–GL nanofibers exhibited a mean diameter of 151 ± 28 nm, and upon the addition of 2, 4, or 6% Sc, the diameter of the nanofibers increased to 230.8 ± 28.4 nm, 236.9 ± 35.35 nm, and 253.07 ± 44.54 nm, respectively. This could be attributed to the increase in the viscosity of the polymer solution upon increasing the concentration of Sc extract. The diameter of the fiber tends to increase in proportion to the square of the viscosity of the polymer solution, yielding thicker fibers.[51] For instance, El Fawal *et al.* produced nanofibers loaded with oregano essential oil in a PCL–GL matrix, observing that the increase in the viscosity of the essential oil increases the diameter of the nanofibers. This could be attributed to the reduced electrical conductivity of the polymer solution following the addition of the essential oil.[52] Similarly, Unalan *et al.* demonstrated that the diameter of the PCL–GL nanofibers increased with the incorporation of clove essential oil.[53] Fig. 1 shows the SEM images of the nanofibers and the diameter distribution curves of free PCL–GL, PCL–GL-2% Sc, PCL–GL-4% Sc, and PCL–GL-6% Sc.

The FFT analysis of the SEM images of the free and loaded nanofibers was conducted using ImageJ, and the corresponding FFT spectra are displayed in the bottom-right corner of each SEM image (Fig. 1(A-1)–(D-1)). For isotropic patterns (random orientation), the FFT spectrum appeared with uniform bright circular features. In contrast, streaks or elongated bright features in the FFT spectrum indicated that the nanofibers have a degree of alignment along specific directions.[35] PCL–GL (Fig. 1(A-1), lower right corner) exhibited a diffuse, circular pattern, indicating an isotropic distribution of fibers. In the lower right corner of Fig. 1(B-1), PCL–GL-2% Sc revealed a slightly less diffuse pattern with elongated features, suggesting a minor degree of fiber alignment. For PCL–GL-4% (Fig. 1(C-1), lower right corner), the FFT spectrum showed pronounced streaks, reflecting a higher degree of directional alignment in the fibers. In Fig. 1(D-1), lower right corner, a similar pattern was observed as the previous image, confirming strong directional alignments in the nanofiber network.

To further quantify the alignment of PCL–GL, PCL–GL-2% Sc, PCL–GL-4% Sc, and PCL–GL-6% Sc, the directionality plugin in ImageJ/Fiji was used. The distribution of fiber orientations within the angle range of 0° to 180° was plotted against the frequency domain.[54] All nanofibers exhibited multidirectional patterns, and we focused in our analysis on the most dominant direction.[35,55] In PCL–GL (Fig. 1; A-3), the dominant direction value was 17.798 with low dispersion (1.13°) and moderate coherency (0.199). This indicated that while some nanofibers are aligned along the dominant direction, the overall structure is largely isotropic with random fiber orientation. In contrast, a sharper peak with a dominant direction of 21.02° was noted in PCL–GL-2% Sc (Fig. 1; B-3). It exhibited an increase in dispersion (2.98°), and a slight reduction in coherency (0.164), reflecting moderate alignment with some variability. With an increased concentration of Sc in PCL–GL-4% Sc (Fig. 1; C-3), a larger dispersion (10.40°) and improved coherency (0.191) were noted. The sharp dominant peak at 28.00° in the frequency plot indicated a strong fiber alignment, mimicking the anisotropic extracellular matrix (ECM) structure.[56] On the other hand, PCL–GL-6% Sc (Fig. 1; D-3), with a dominant direction of 15.38°, reduced dispersion (2.91°), and lower coherency (0.169), exhibited some loss of alignment consistency. Secondary peaks in the frequency plot suggested the emergence of structural heterogeneity due to fiber aggregation or overloading.[57] While still better aligned than PCL–GL, it is less consistent than the PCL–GL-4% Sc nanofiber due to its lower coherency and increased structural heterogeneity, as indicated by secondary peaks in the frequency plot.[57]

3.2.2. FTIR. The FTIR spectrum of the Sc extract revealed characteristic peaks indicating the presence of phenolic, acidic, and alcoholic groups. Specifically, the FTIR peaks included 892 cm^{-1} (aromatic bending), 1146.2 cm^{-1} (C–O stretching), 1290 cm^{-1} (sulfonate group), 1382 cm^{-1} (alkane C–H bending), 1663 cm^{-1} (aromatic C–H bending), and a broad absorption peak at 3467 cm^{-1} (O–H group).[58]

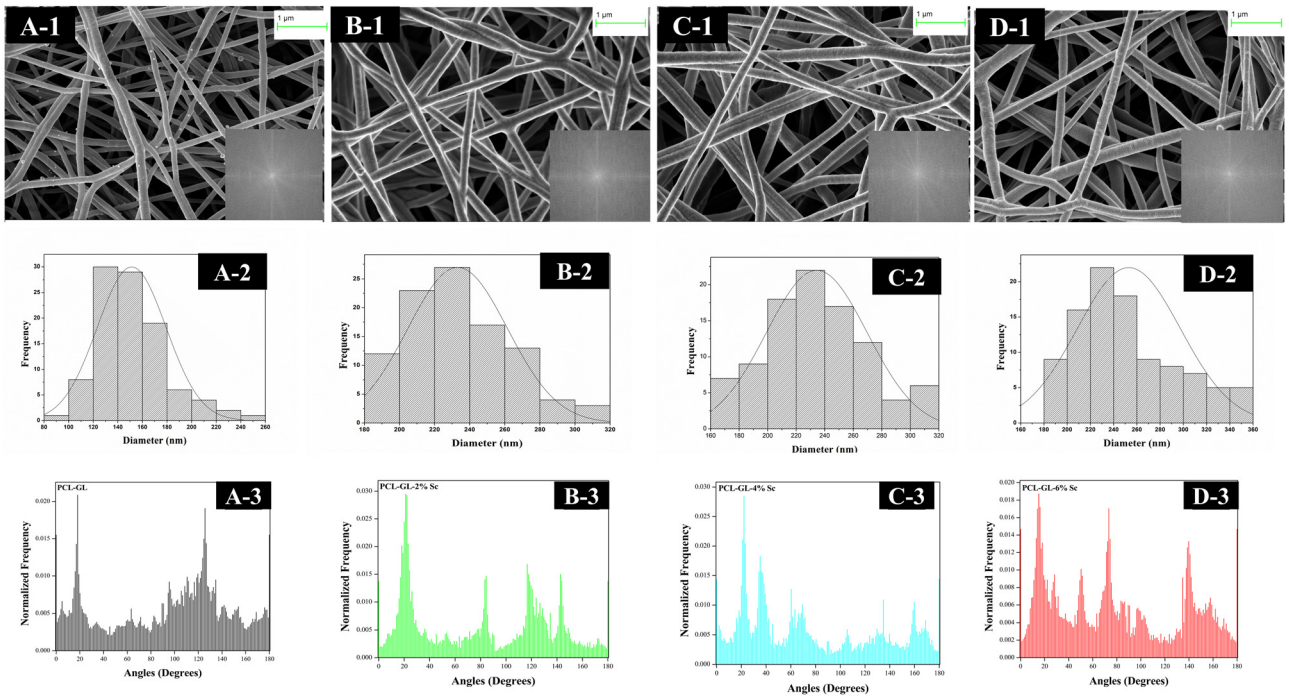

Fig. 1 SEM images, diameter distribution curves, FFT analysis, and directionality plots of various nanofiber samples. The SEM images are taken at a scale of 1 μm and illustrate the morphology of the following (A-1) PCL–GL (151± 28 nm), (B-1) PCL–GL-2% Sc (230.8 ± 28.4 nm), (C-1) PCL–GL-4% Sc (236.9 ± 35.35 nm), and (D-1) PCL–GL-6% Sc (253.07 ± 44.54 nm). In the lower-right corners of each SEM image, FFT spectra are presented. A-1, lower right corner shows a diffuse circular feature of PCL–GL, reflecting an isotropic pattern, while B-1, C-1, and D-1, in the lower right corner show the FFT spectra of PCL–GL-2% Sc, PCL–GL-4% Sc, and PCL–GL-6% Sc, respectively, having moderate elongated streaks that indicate fiber alignment. Below each SEM image, the diameter distribution curves are shown, representing the size distribution for the respective samples: (A-2) PCL–GL, (B-2) PCL–GL-2% Sc, (C-2) PCL–GL-4% Sc, and (D-2) PCL–GL-6% Sc. Below each distribution curve are directionality plots of nanofiber orientations (0°–180°). (A-3) shows random alignment with low dispersion and moderate coherency of PCL–GL, while PCL–GL-2% Sc (B-3) displays moderate alignment. PCL–GL-4% Sc (C-3) achieves the strongest alignment with high directionality, larger dispersion, and improved coherency. PCL–GL-6% Sc (D-3) exhibits reduced alignment due to heterogeneity.

On the other hand, the FTIR spectrum of the PCL–GL nanofibers showed characteristic peaks for PCL at 1733 cm^{-1} (C═O stretching), 1105 cm^{-1} (C–O stretching), and 2923 cm^{-1} (H–C–H stretching).[59] Furthermore, it exhibited characteristic GL peaks at 1646 cm^{-1} (C═O stretching of primary amide I), 1561 cm^{-1} (C–N stretching of amide II and III), and 1572 cm^{-1} (N–H bending).[59]

Upon incorporating the Sc extract into the PCL–GL nanofibers, the FTIR spectrum exhibited overlapping, shifting, and variations in peak intensities. These changes could be attributed to hydrogen-bonding interactions between the carbonyl groups in the Sc extract and the amine groups in GL.[59] This aligns with the findings of Azizi *et al.*, who demonstrated that incorporating *Calendula officinalis* extract into the PCL–GL nanofibers resulted in the emergence of new peaks or shifts in existing peaks in the FTIR spectra, indicating the presence of various functional groups from the extract.[31] Fig. 2A presents the FTIR spectrum of free Sc extract, PCL–GL, and PCL–GL-6% Sc.

3.2.3. X-ray diffraction of the nanofibers. Examining the XRD patterns of PCL pellets, GL powder, PCL–GL, and PCL–GL-6% Sc nanofibers revealed distinct characteristics, as shown in Fig. 2B. GL powder, characterized as an amorphous polymer, exhibited no peaks in the XRD pattern.[60] In contrast, the crystalline polymer PCL displayed two peaks at 2θ values of 21.23° and 24.35°.[61] The XRD pattern of the PCL–GL scaffold retained the typical peaks of PCL but with a reduced intensity attributed to interactions between molecules of amorphous GL and crystalline PCL polymers. Similar findings were reported by Gautam *et al.*, where the peak intensities of the PCL nanofibers decreased after the incorporation of chitosan.[62] Interestingly, the addition of Sc had an insignificant shift in the diffraction pattern of PCL–GL. This suggests the likely incorporation of Sc within the PCL–GL scaffold, which is in agreement with findings of previous reports.[52,63–65] Likewise, El Fawal *et al.* reported comparable findings in PCL–GL nanofibers loaded with oregano oil.[52]

3.2.4. Thermal stability. For the TGA analysis, Fig. 2C presents derivative thermogravimetric analysis (DTG) plots performed on PCL pellets, GL powder, Sc extract, PCL–GL, and PCL–GL-6% Sc nanofibers, revealing distinctive thermal degradation profiles.

The PCL pellets exhibited a single degradation stage from 297–500 °C, resulting in an 86.4% weight loss. On the other hand, GL displayed a dual-stage degradation process: an initial stage (49–100 °C) involving water loss and a subsequent stage (240–425 °C) with protein chain and peptide bond breakage, reaching peak degradation at 322 °C. PCL–GL nanofibers exhibited a singular degradation phase from 290 to 435 °C,

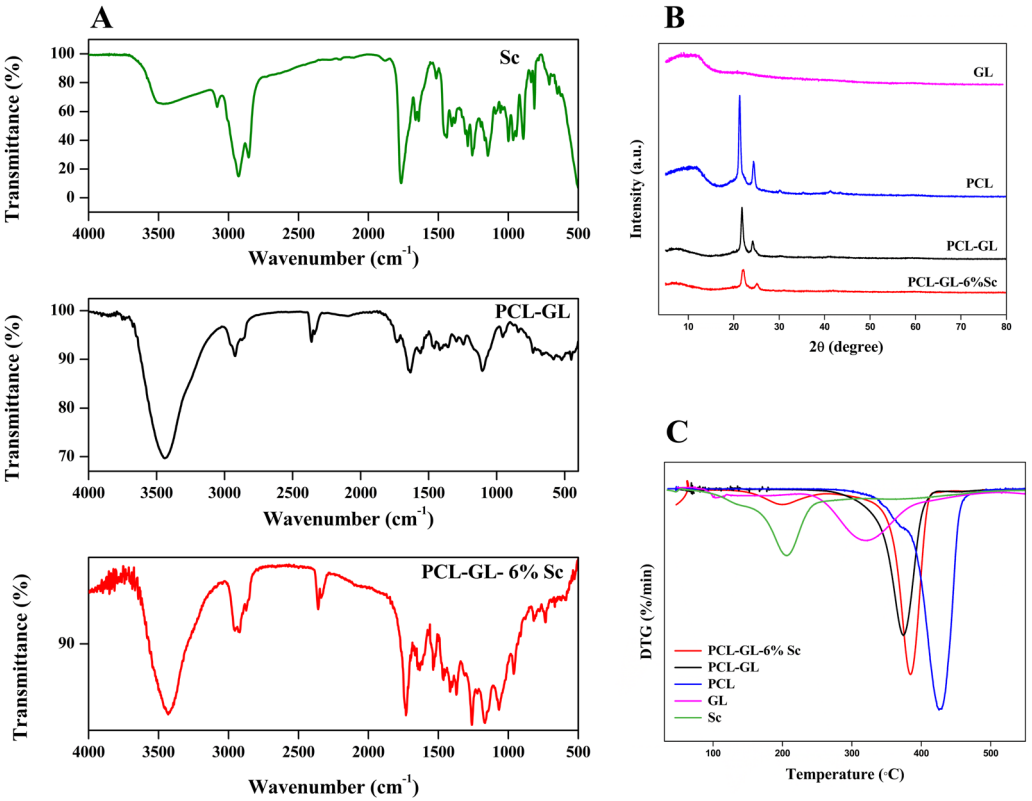

Fig. 2 Comprehensive characterization of the PCL–GL nanofibers *via* assessment of their chemical, physical, and thermal characteristics. (A) FTIR spectra of the Sc extract, PCL–GL, and PCL–GL-6% Sc nanofibers, displaying the characteristic functional groups and bonding interactions. (B) XRD plot of the PCL pellets, GL powder, PCL–GL, and PCL–GL-6% Sc nanofibers. (C) DTG thermogram of the PCL pellets, GL powder, Sc extract, PCL–GL, and PCL–GL-6% Sc nanofibers to illustrate the decomposition behavior.

peaking at 375 °C, suggesting improved heat resistance and thermal stability due to polymer interactions. The Sc extract exhibited a dual-step degradation pattern, with stages at 49–140 °C and 160–260 °C, and a maximum degradation at 204 °C. The first stage was attributed to water and solvent loss. PCL–GL-6% Sc nanofibers displayed peaks at 200 °C (Sc components) and 384 °C (PCL–GL chain degradation). The decline of the first stage in Sc in the nanofibers suggested the absence of small molecules like water and solvent in the nanofibers. These findings align with previous studies on the thermal degradation of nanofiber scaffolds.[37,66–68]

3.2.5. Tensile strength. Fig. 3A presents a stress/strain plot of free PCL–GL nanofibers and loaded ones (PCL–GL-2% Sc, PCL–GL-4% Sc, and PCL–GL-6% Sc nanofibers) showing the tensile strength of the formed nanofibers. Table 2 presents Young's modulus, yield strength, elongation at break, and ultimate tensile strength of the free and loaded nanofibers.

Generally, the smaller the diameter of the nanofibers, the better the tensile properties they display. Consequently, free PCL–GL nanofibers, which have the smallest diameters, demonstrated the highest resistance to elastic deformation, with Young's modulus of 10 ± 1.23 MPa.[69,70] The introduction of Sc extract increased the diameter of the nanofibers, resulting in a decrease in Young's modulus.[71] This observation aligns with Borges-Vilches *et al.* findings, where the addition of the *Pinus radiata* extract to the PCL–GL nanofibers reduced their mechanical strength.[30]

Conversely, the yield strength of the nanofibers improved with increasing concentrations of Sc extract. Free PCL–GL has a yield strength of 0.162 ± 0.05 MPa, which increases to 0.250 ± 0.78 MPa for PCL–GL-2% Sc and 0.289 ± 0.04 MPa for PCL–GL-4% Sc, peaking at 0.409 ± 1.52 MPa for PCL–GL-6% Sc. This suggests that the Sc extract may enhance internal bonding within the nanofiber structure.[72,73] The elongation at break of the PCL–GL nanofibers increases with the addition of Sc extract up to 4%, but shows a slight decrease at 6%, indicating some reduction in flexibility. The ultimate tensile strength shows a peak at 1.237 ± 0.001 MPa for the PCL–GL composite containing 2% Sc, which indicates enhanced mechanical stability relative to the base PCL–GL. However, the strength decreases with higher concentrations, reaching 0.563 ± 0.124 MPa at 6% Sc, possibly due to the interference of the extract with the polymer network resulting in weak spots and reduction of the tensile strength of the material.[74]

3.2.6. Contact angle of the nanofibers. While using PCL alone for wound healing is not ideal due to its hydrophobic nature, incorporating GL significantly enhances its hydrophilicity owing to the presence of carboxyl and amine functional groups, making it more suitable for wound dressing applications.[75] Additionally, the inclusion of ethanolic

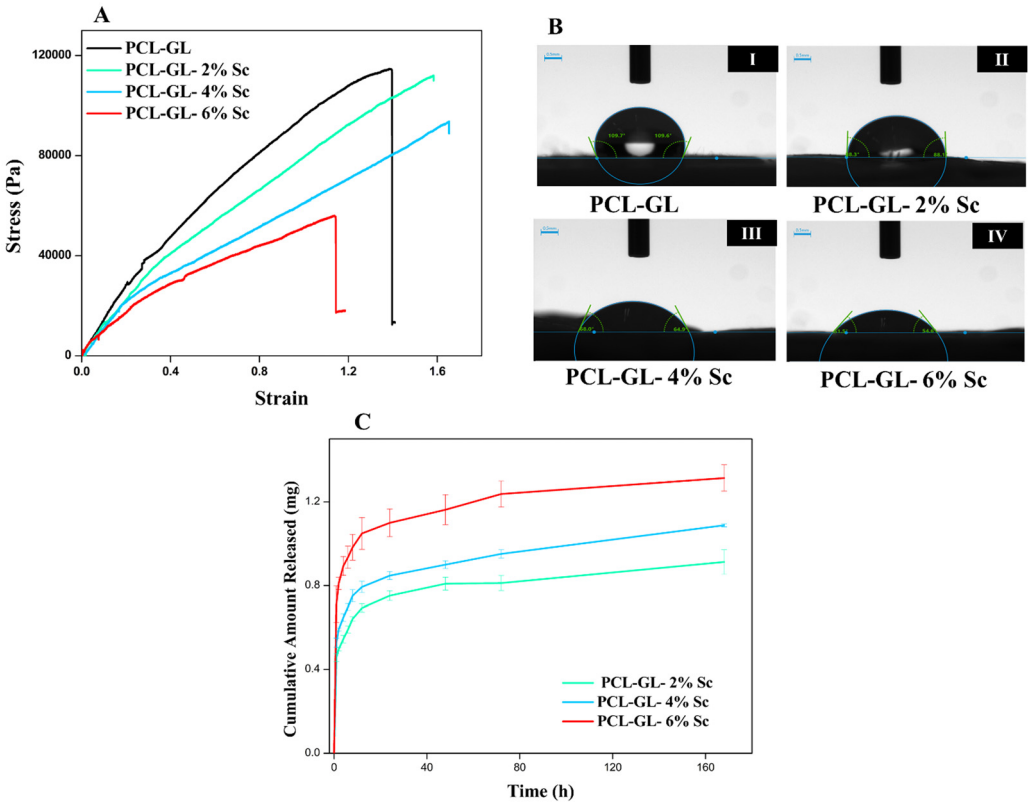

Fig. 3 Mechanical properties, contact angle, and release profile of PCL–GL nanofibers with varying concentrations of Sc extract. (A) Stress–strain curves of PCL–GL, PCL–GL-2% Sc, PCL–GL-4% Sc, and PCL–GL-6% Sc nanofibers, showing a decrease in stiffness and an increase in the initial resistance to deformation at higher Sc extract levels. (B) Water contact angle measurements of (I) PCL–GL: 109.78° ± 1.23, (II) PCL–GL-2% Sc: 88.81° ± 1.23, (III) PCL–GL-4% Sc: 68.0° ± 3.32, and (IV) PCL–GL-6% Sc: 54.6° ± 2.03, demonstrating an improvement in the hydrophilicity with the increase of Sc concentration. (C) Cumulative release of Sc extract over 7 days for the nanofibers: PCL–GL-2% Sc, PCL–GL-4% Sc, and PCL–GL-6% Sc, showing enhanced release with increasing Sc concentration.

Table 2 Tensile strength properties of free and loaded nanofibers

	Young's modulus (MPa)	Yield strength (MPa)	Elongation at break (%)	Ultimate tensile strength (MPa)
PCL–GL	10 ± 1.23	0.162 ± 0.05	14.114 ± 4.2	1.146 ± 0.003
PCL–GL-2% Sc	10 ± 0.05	0.250 ± 0.78	16.397 ± 0.1	1.237 ± 0.001
PCL–GL-4% Sc	6 ± 1.22	0.289 ± 0.04	16.857 ± 2.9	0.934 ± 0.002
PCL–GL-6% Sc	4 ± 0.74	0.409 ± 1.52	12.691 ± 3.7	0.563 ± 0.124

extract of Sc further enhances the hydrophilicity of the composite.

Hydrophilicity and hydrophobicity were quantitatively assessed through water contact angle measurements, as depicted in Fig. 3B. The PCL–GL nanofibers exhibited a water contact angle of 109° ± 0.02, indicating a relatively hydrophobic surface. However, the addition of Sc extract significantly reduced the contact angle, demonstrating enhanced hydrophilicity to 88.81° ± 1.23, 68.0° ± 3.32, and 54.6° ± 2.03, respectively. A similar decrease in contact angle was observed in the study by Adeli-Sardou *et al.*, where the incorporation of Lawsone into PCL–GL reduced the water contact angle.[71] These results are consistent with previously reported data.[37,71] This improvement in hydrophilicity is crucial for wound healing applications as it could enhance cell attachment, proliferation, and overall biocompatibility of the dressing material.[76]

3.2.7. *In vitro* drug release profile. An important parameter of wound dressings is their ability to release their drug cargo in a controlled manner.[77] The Sc extract content released from the prepared nanofibers was measured over 7 days, showing a triphasic pattern. Initially, a burst release occurred, marked by a significantly high release rate, attributed to the accumulation of Sc molecules on the surface of the polymeric system. Within the first 12 h, the release percentages of Sc were 57.76 ± 1.68, 37.69 ± 1.29, and 36.72 ± 2.66% from PCL–GL-2% Sc, PCL–GL-4% Sc, and PCL–GL-6% Sc, respectively.

In the subsequent phase, a slower release rate indicated drug release due to mild polymer degradation or chain

breakage, representing a controlled release mechanism. After 72 h, the release percentage increased to reach 70.52 ± 3.05, 45.18 ± 0.94, and 43.33 ± 2.17% from PCL–GL-2% Sc, PCL–GL-4% Sc, and PCL–GL-6% Sc, respectively. Notably, the nanofiber with the lowest Sc concentration (2%) demonstrated the highest percentage release rate, potentially due to changes in the physical structure of the nanofiber matrix at higher concentrations, leading to increased density, which can impede the diffusion of extract molecules within the matrix.[78,79]

The third phase involved bulk erosion as the polymer continued to hydrate, displaying a slower release rate compared to the earlier stages due to the time required for bulk erosion. On day 7 (168 h) the release percentage reached 79.47 ± 4.98, 51.69 ± 0.349, and 45.99 ± 2.16% in PCL–GL-2% Sc, PCL–GL-4% Sc, and PCL–GL-6% Sc, respectively.[80,81] Fig. 3C presents the Sc released from PCL–GL nanofibers loaded with different Sc concentrations (2, 4, and 6%).

3.2.8. Release kinetics of Sc extract from the nanofibers. In this study, a comprehensive analysis using various mathematical models was conducted to understand the release kinetics of Sc extract in the initial 12 hours from PCL–GL-2%, PCL–GL-4% Sc, and PCL–GL-6% Sc nanofibers. The employed models included zero-order kinetics, first-order kinetics, the Hixson model, the Higuchi model, and the Korsmeyer–Peppas model. Fig. S2 in the ESI† depicts the kinetic model plots. Furthermore, Table 3 summarizes the key parameters of the release kinetics of Sc extract from the synthesized nanofibers, highlighting the correlation coefficient (R^2) values.[41]

The release kinetics of the Sc extract were found to align with the Higuchi model, showing the highest correlation coefficient (R^2) values across all nanofiber samples. This finding suggests that the release mechanism is predominantly driven by diffusion through the polymer matrix. Despite the crystallinity of PCL, which typically creates diffusion barriers, the incorporation of GL, hydrophilic in nature, into the nanofibers facilitated the diffusion of Sc from the nanofiber due to its rapid swelling and porous structure.[82,83] Moreover, this synergistic effect between PCL and GL enabled sustained and controlled release of Sc extract over time. These results are consistent with a previous study, where Altun *et al.* underscored the beneficial role of adding a hydrophilic polymer such as cellulose in modifying the release kinetics of nanofiber-based delivery systems.[84] To further identify the type of Sc release mechanism, the release exponent (n) in the Korsmeyer–Peppas model was calculated. The data revealed that all the nanofibers follow Fickian diffusion as $n \leq 0.45$, in accordance with previously reported data.[41,66]

Table 3 Mathematical models of Sc release kinetics and R^2 of PCL–GL-2% Sc, PCL–GL-4% Sc, and PCL–GL-6% Sc nanofibers. $n \leq 0.45$ suggests adherence to Fickian diffusion

	Zero-order	First-order	Higuchi	Hixson	Korsmeyer–Peppas
	R^2				n
PCL–GL-2% Sc	0.9743	0.9888	0.9978	0.9846	0.1794
PCL–GL-4% Sc	0.9368	0.9482	0.9891	0.9445	0.1647
PCL–GL-6% Sc	0.9069	0.9218	0.9756	0.917	0.1519

3.3. *In vitro* biological activities of PCL–GL-Sc nanofibers

3.3.1. Antimicrobial assessment. An AlamarBlue assay was employed to determine the MIC using the microdilution method. In its oxidized form, AlamarBlue (resazurin) appears blue. However, when bacteria are metabolically active and viable, they generate nicotinamide adenine dinucleotide (NADH) and nicotinamide adenine dinucleotide phosphate (NADPH) as metabolic byproducts. These byproducts can then reduce resazurin into resorufin, causing a color change from blue to pink. Consequently, the concentration of the extract that did not induce any color change was identified as the MIC. The ethanolic extract exhibited a MIC of 6%. The antimicrobial assay demonstrated significant inhibitory effects of the Sc extract against *P. aeruginosa*, *S. aureus*, and *E. coli*, aligning with the literature findings where Ahmed *et al.* showed that the methanolic extract of Sc was effective against *S. aureus*.[85] Omer *et al.* also showed that the ethanolic extract of Sc exhibited an inhibition zone of 18–20 mm against *S. aureus*.[86] Furthermore, Alaagib and Ayoub reported the remarkable activity of Sc against *E. coli*, *P. aeruginosa*, and *S. aureus*.[87] The observed antimicrobial activity could be attributed to the presence of bioactive constituents in the extract that were reported previously for their antimicrobial activities.[88]

The ISO 20743:2021 protocol for antimicrobial activity in fabrics focuses on contact-based antibacterial efficacy. This directly aligns with the goal of this study, which is to evaluate how effectively the nanofibers eliminate bacteria through direct contact with an infected wound.[43] Fig. 4A represents the log reduction values of *P. aeruginosa*, *S. aureus*, and *E. coli* treated with nanofibers loaded with different concentrations of Sc (2%, 4%, and 6%). The results have shown that all tested bacteria were inhibited in a dose-dependent manner as the concentration of Sc in the nanofibers increased. Notably, *S. aureus* showed the most significant reduction in bacterial count, highlighting its higher susceptibility to the antimicrobial effects of the Sc extract.

Among the formulations, PCL–GL-6% Sc achieved the highest log reductions for all bacteria, with an approximate log reduction of 7, equivalent to 99.999% of the control. This level of reduction is crucial in preventing infections, as a clean wound environment encourages the growth of fibroblasts to ensure effective tissue regeneration and wound closure.[89] Eremanthine, a hydrophobic sesquiterpene and the most abundant compound in our Sc extract, was reported to integrate into bacterial lipid bilayers and disrupt the membrane integrity, causing leakage of cytoplasmic contents.[90] This mechanism likely contributes to the strong antimicrobial activity observed, particularly against Gram-positive bacteria (*S. aureus*), whose thicker peptidoglycan layer is more susceptible to the effects of eremanthine.[91] In addition, dehydro-saussurea lactone targets bacterial enzymes like DNA gyrase and topoisomerase, which are essential for DNA replication.[91] Furthermore, integrating bioactive natural compounds into nanofibers has been associated with enhanced antimicrobial activities as they effectively prevent the formation of biofilms and inhibit the development of antibiotic resistance.[92] For example, a study by Fallah *et al.* demonstrated that incorporating curcumin into PCL–GL

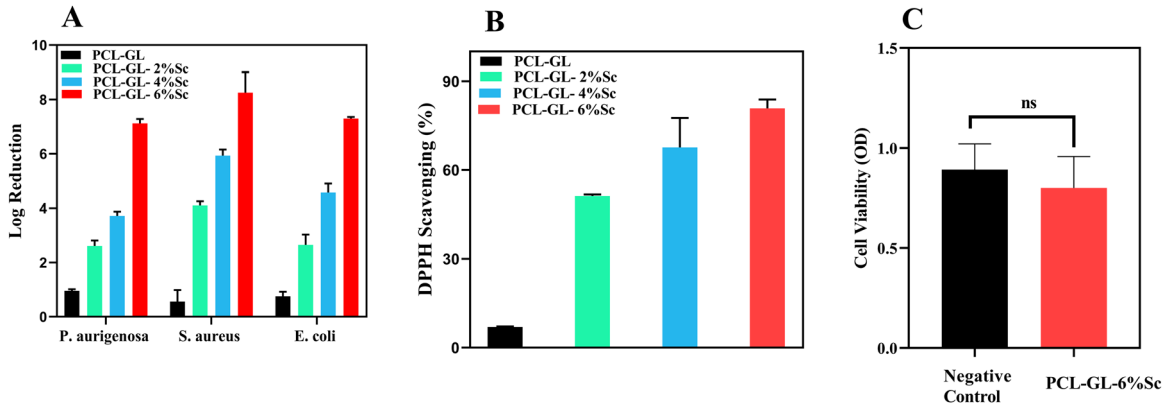

Fig. 4 Antimicrobial, antioxidant, biocompatibility assay, and morphological assessment of HSF cells. (A) The log reduction values of *P. aeruginosa*, *S. aureus*, and *E. coli* after treatment for 24 h with Sc-loaded nanofibers (2%, 4%, and 6%) and free PCL–GL, showing the highest reduction with PCL–GL-6% Sc. (B) The DPPH scavenging activity percentage upon treatment of HSF cells with nanofibers loaded with different concentrations of Sc (2%, 4%, and 6%) and free PCL–GL. (C) Cell viability assessment of HSF cells treated with PCL–GL-6% Sc nanofibers *vs.* untreated control group (data are represented as mean ± SD, n = 5 per group), showing no significant difference (ns: non-significant, $p > 0.05$).

nanofibers resulted in a 99.9% antibacterial efficacy against methicillin-resistant *S. aureus*.[93]

3.3.2. Free-radical scavenging efficiency of the PCL–GL-Sc nanofibers. The antioxidant activity of the nanofibers was assessed using the DPPH assay. Sc extract, rich in polyphenolic compounds, demonstrated strong free radical scavenging capabilities.[3,87] When incorporated into the PCL–GL nanofibers at concentrations of 2%, 4%, and 6%, the DPPH scavenging activity was 51.17%, 67.61%, and 80.85%, respectively, as shown in Fig. 4B. This significant antioxidant activity suggests that the Sc-loaded PCL–GL nanofibers can effectively scavenge reactive oxygen species, crucial for promoting and accelerating the wound healing process.[13,94] Du *et al.* showed that incorporating arbutin into the PCL–GL nanofibers enhanced their ability to scavenge reactive oxygen species, crucial for accelerating wound healing.[95]

3.3.3. Biocompatibility assessment. Wound dressings should be assessed with regard to their biocompatibility to ensure lack of adverse reactions (such as inflammation or toxicity) upon application to wounds.[96] For this purpose, a direct MTT assay was performed to assess the cytotoxicity of PCL–GL-6% Sc nanofibers on HSF cells. Cells were incubated with the nanofibers for 24 h, and the OD of the formazan crystals was measured at 570 nm. A negative control (untreated cells) was used as a reference for cell viability. The results indicate that HSF treated with PCL–GL-6% Sc nanofibers showed no significant reduction in viability compared to the untreated control group (ns, $p > 0.05$), as shown in Fig. 4C. These findings suggest that PCL–GL-6% Sc nanofibers are biocompatible and support cell viability, making them promising candidates for wound healing applications. These findings are consistent with the study of Lim and Sultana who confirmed the biosafety of PCL–GL nanofibers coated with silver for HSF cells. The OD values of the formazan product formed in the MTT assay on HSF control (untreated) cells and cells treated with nanofibers showed no significant difference, confirming the biocompatibility of the nanofibers to HSF cells.[97] In another study, PCL–GL nanofibers showed no significant cytotoxicity to HSF cells, where high absorbance values in the MTT assay after treatment with PCL–GL nanofibers indicated enhanced cell proliferation and viability.[98]

3.4. *In vivo* wound healing

3.4.1. Comprehensive evaluation of wound closure and leukocyte dynamics. This study evaluated the healing effects of the daily application of PCL–GL-6% Sc nanofibers on wounds by assessing the wound closure percentage, weight changes in rats, and leukocyte dynamics after 14 days, as shown in Fig. 5. Wound closure percentages were measured daily, revealing that the PCL–GL-6% Sc treated group exhibited a significantly faster healing rate compared to the negative control group (injured but untreated), as shown in Fig. 5A. The wound closure percentage on day 7 in the control group increased to 13.33 ± 9.4%, suggesting relatively slow healing progress when compared to the treated group that exhibited a closure percentage of 30 ± 6.3% ($p \leq 0.01$). This dramatic difference in wound closure percentages emphasizes the effectiveness of PCL–GL-6% Sc. The treated group achieved nearly double the wound closure percentage compared to the control group within just one week. Such advancements are crucial in clinical applications for optimizing wound management and recovery. After 14 days, the treated group achieved an average wound closure of 82.22 ± 4.96%, whereas the control group showed only 68.88 ± 7.37% closure, indicating the efficacy of the treatment in enhancing wound repair ($p \leq 0.01$).[99,100]

In terms of weight changes, all groups: (a) PCL–GL-6% Sc-treated, (b) negative control (injured but untreated), and (c) normal (uninjured), exhibited a similar trend of increased weight measured on day 14 compared to day 0, as shown in Fig. 5B. The treated group maintained a stable and healthy weight gain, with an initial average weight of 117.33 ± 2.05 g and a final weight of 167.67 ± 7.40 g. The normal (uninjured) group also experienced weight gain, following a similar pattern. This suggests that the nanofiber treatment did not have any adverse effects on the health and metabolism of the rats. Moreover, the control group exhibited similar trends, where

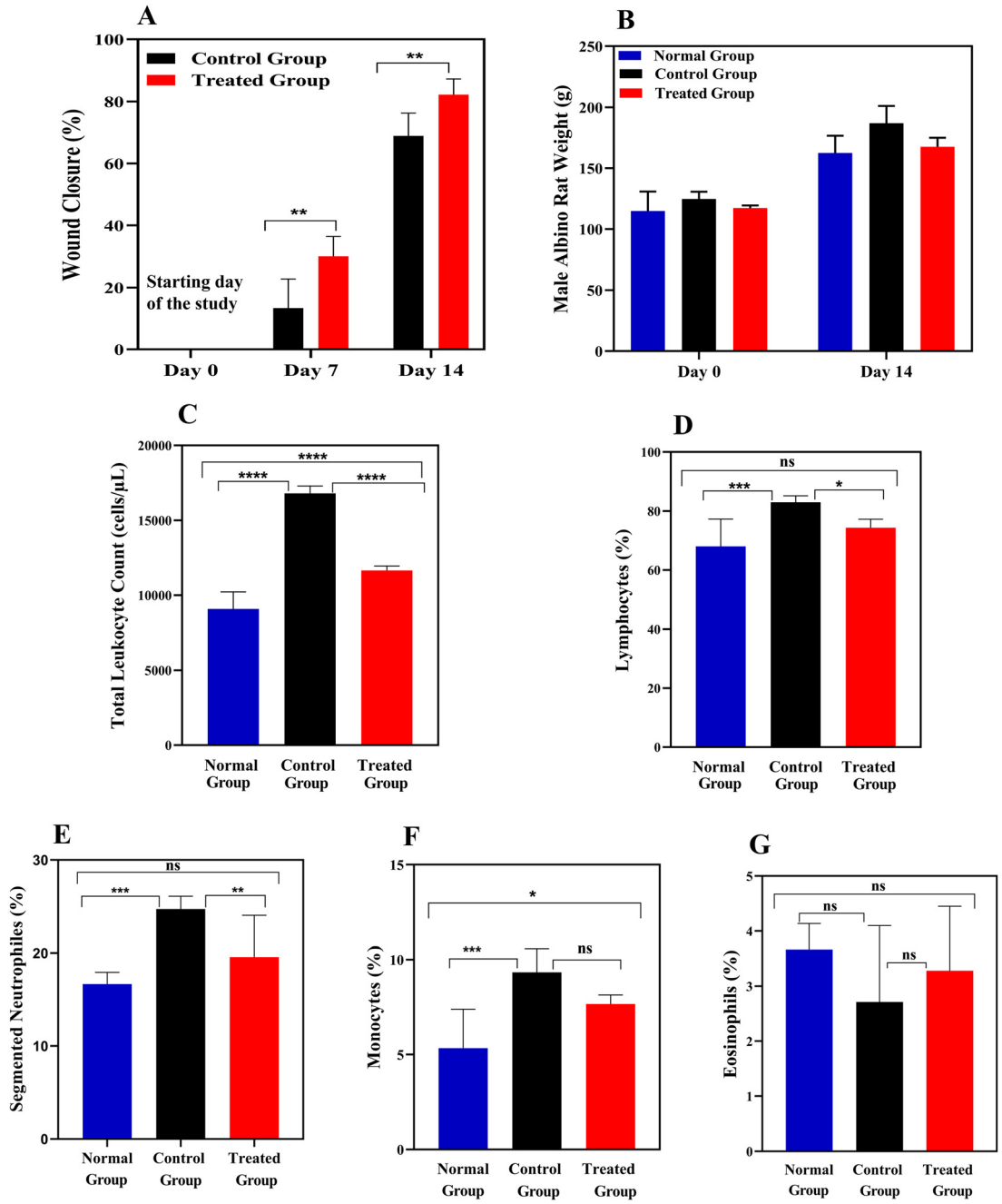

Fig. 5 Analysis of healing progress and immune response dynamics. The data are presented as mean ± SE (n = 7). For statistical analysis, one-way ANOVA was used, followed by Tukey's test. Statistical significance was assigned as follows: $p \leq 0.05$ was considered significant and marked as *, $p \leq 0.01$ as **, $p \leq 0.001$ as ***, and $p < 0.0001$ as ***; non-significant results were denoted as ns. (A) Wound closure percentages indicate that the treated group exhibited a significantly faster healing rate compared to the negative control group. (B) Weight changes of rats on days 0 and 14 showed a similar trend of weight increase across all groups. (C) TLC levels in the normal, control, and PCL–GL-6% Sc-treated groups, highlighted significant differences across these groups. (D) Lymphocyte levels in the normal, control, and treated groups, with a significant difference observed between PCL–GL-6% Sc treated and control groups. (E) Segmented neutrophil levels in the normal, control, and treated groups, with no significant difference, were observed between the PCL–GL-6% Sc treated and normal groups. (F) Monocyte levels in the normal, control, and PCL–GL-6% Sc-treated groups, underscored the role of macrophages in wound healing, with treated groups showing a transition from the inflammatory to the proliferative phase. (G) Eosinophil levels in the normal, control, and PCL–GL-6% Sc-treated groups, indicate that the eosinophil levels remain relatively consistent and unaffected by the nanofiber treatment.

the starting weight was at 124.85 ± 5.79 g and ended at 187.90 ± 14.22 g, showing that the experimental conditions mimicked normal growth.

White blood cells (WBC) are involved in inflammation, tissue formation, and remodeling stages of wound healing. Each stage involves distinct types of WBC that contribute to the

healing process. Fig. 5C presents total leukocyte count (TLC) in the normal, negative control, and PCL–GL-6% Sc treated groups. In the normal group, TLC remains within the reference range of 9100 ± 1122.49 cells per μL, indicating no inflammatory response. In contrast, the control (injured) group exhibits elevated TLC of 16 800 ± 498.89 cells per μL, signifying ongoing inflammation due to untreated wounds ($p < 0.0001$). The PCL–GL-6% Sc treated group shows a reduced TLC (11650 ± 300 cells per μL) and a significant difference compared to the control ($p < 0.0001$), indicating that the treatment effectively mitigates inflammation.[101]

The lymphocyte levels in the normal, negative control, and PCL–GL-6% Sc treated groups are shown in Fig. 5D. Their count percent in the PCL–GL-6% Sc treated group (68 ± 9.24%) showed no significant difference when compared to the normal group (74.33 ± 2.86%), suggesting that there is no ongoing infection at the wound site. The control group, however, displayed elevated lymphocyte counts and persistent inflammation (83 ± 2.16%), indicating a significant difference when compared to the treated group ($p < 0.05$).

Furthermore, Fig. 5E depicts segmented neutrophil levels in the normal, negative control, and PCL–GL-6% Sc treated groups. The count percent of segmented neutrophils in the PCL–GL-6% Sc treated group (19.57 ± 4.48%) showed no significant difference when compared to the normal group (16.66 ± 1.24%), suggesting that PCL–GL-6% Sc nanofibers helped resolve inflammation more rapidly.[102] The control group, however, displayed elevated neutrophil counts (24.71 ± 1.38%) indicative of an acute inflammatory response, when compared to the treated group ($p \leq 0.01$).[102]

Monocyte counts relative to TLC in all groups are displayed in Fig. 5F. The count percent in the normal group is within the standard range (5.33 ± 2.05%), showing a significant difference ($p \leq 0.05$) when compared to the treated group (7.66 ± 0.47%), and negative control group (9.33 ± 1.24%). The treated group exhibited a lower monocyte count than the control group, indicating a transition from the inflammatory phase to the proliferative phase as the need for inflammation decreases, leading to a reduction in monocyte and macrophage activity.[101]

Eosinophil counts relative to TLC in the normal, negative control, and treated groups are shown in Fig. 5G. The levels in the normal group are 3.66 ± 0.47%. In both the control and treated groups, eosinophil levels show minimal variation compared to the normal group, indicating that the treatment does not significantly affect these cells, typically abundant in allergic reactions. These results are consistent with previously reported counts of leukocytes measured during the wound healing process.[103,104]

3.4.2. qRT-PCR for gene expression. Wound tissue samples from both the negative control and PCL–GL-6% Sc-treated groups were utilized to elucidate the genetic expression profiles involved in inflammatory responses, cell death pathways, and tissue repair processes. For this purpose, the genetic expression of inflammatory mediators, including interleukins (IL-1, IL-6, IL-12) and tumor necrosis factor-alpha (TNF-α) was evaluated, as depicted in Fig. 6A. The results show that the fold expression of inflammatory mediators (TNF-α, IL-1, IL-12) in both groups had no significant difference (1–1.5 fold expression) because the primary phase of inflammation had already resolved by day 14, reflecting a normal progression of the wound healing process. However, IL-6 showed significant downregulation in the treated group ($p \leq 0.05$) compared to the control group. This suggests that the treatment is effectively transitioning the wound from the inflammatory phase to the proliferative phase because IL 6 is involved in the initiation of tissue repair.[105] Furthermore, injured, untreated control wounds may have unresolved microbial infections, leading to chronic inflammation and an increase in IL-6.[106] In contrast, PCL–GL-6% Sc possesses antimicrobial and antioxidant activities that reduce IL-6 gene expression triggered by immune cells.[107]

Regarding apoptosis-related genes, the expression of Bax was significantly higher in the treated group ($p < 0.0001$) compared to the control, while P53 levels remained unchanged. Furthermore, Bcl-2, an anti-apoptotic gene, showed no significant difference (Fig. 6B). These findings strongly suggest that PCL–GL-6% Sc nanofibers promote the removal of damaged cells through apoptosis, which aids in resolving inflammation. They also contribute to appropriate tissue remodeling and mitigate excessive scarring.

The genetic expression of matrix metalloproteinases (MMP-1, MMP-3, MMP-13) was assessed using qRT-PCR. The findings revealed that treatment with PCL–GL-6% Sc resulted in a significant increase in MMP3 gene expression ($p \leq 0.05$), as illustrated in Fig. 6C. In contrast, there was no significant upregulation observed in MMP2 and MMP13 genes compared to the control group. This suggests that PCL–GL-6% Sc promotes angiogenesis and facilitates the formation of new blood vessels to deliver oxygen and nutrients to the wound site, specifically enhancing MMP3 expression.[108]

3.4.3. Histological and immunohistochemical analyses. H&E staining of normal cells (Fig. 7I) showed keratinized cells in the thin epidermis, while the dermis was characterized by adnexal structures (pilosebaceous units), along with fibroblasts and irregular collagen bundles. In contrast, the keratin in Masson's trichrome stain appeared red, while collagen fibers were stained blue in the dermis. Additionally, the smooth muscles in blood vessels were stained red, as depicted in Fig. 7II.

For the histological analysis of the negative control (injured, untreated) skin tissue, H&E staining (Fig. 7III) revealed that the wound tissue was covered by a crust with an absent epidermal layer, indicating early re-epithelialization. In the upper dermis, there was a significant presence of neutrophils with multilobed nuclei, and thin-walled capillaries. The dermis also contained numerous fibroblasts, appearing as spindle-shaped cells with elongated nuclei, and a substantial infiltration of mononuclear cells, including lymphocytes, plasma cells, and macrophages. The ECM in the dermis also appeared loosely organized with minimally defined collagen fibers, presenting a pale pink background, indicative of immature connective tissue formation. On the other hand, Masson's trichrome in Fig. 7IV reveals a prominent, blue-colored crust, indicating collagen

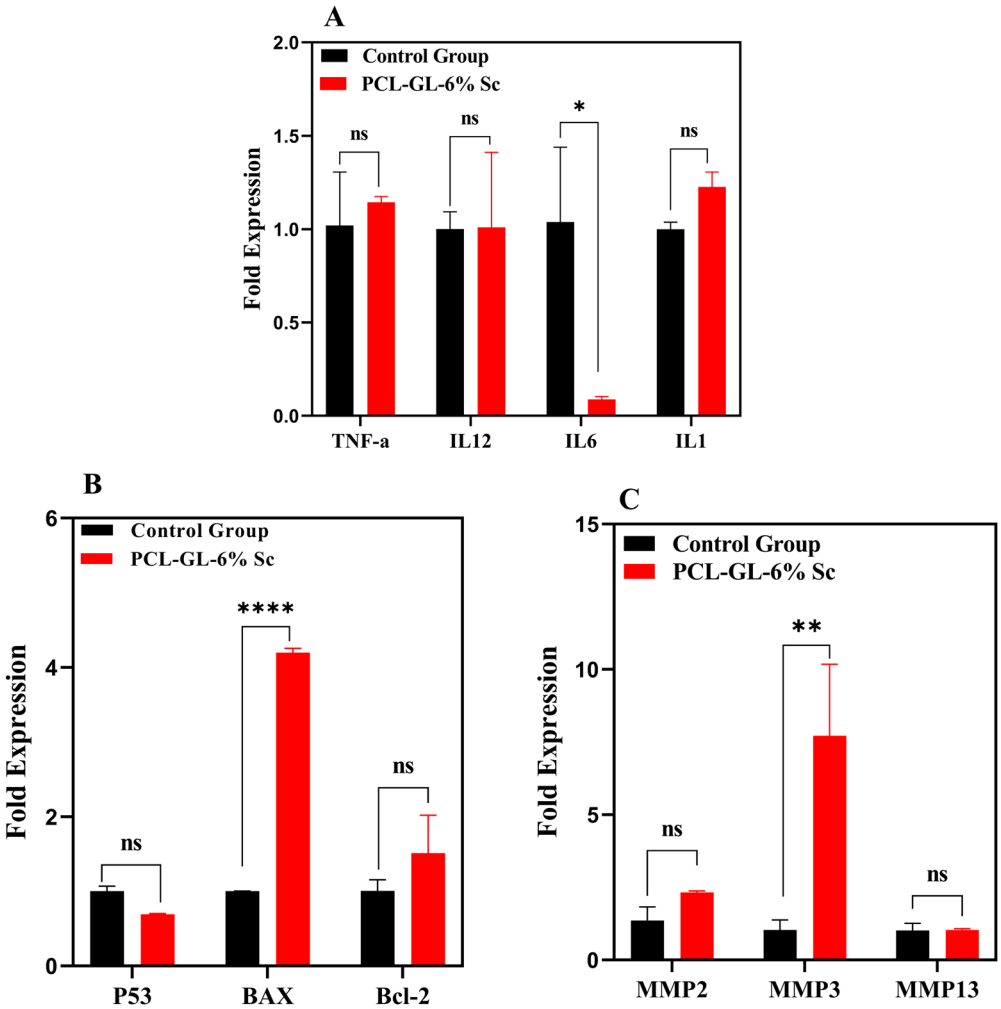

Fig. 6 Genetic expression of inflammatory, apoptotic, and angiogenesis genes using qRT-PCR. Data were expressed as mean ± SE (n = 3), and statistical analysis employed a two-way ANOVA for comparison between the control group and the PCL–GL-6% Sc-treated group. Significance was set at 0.05, with levels of statistical importance denoted as: * for $p \leq 0.05$, ** for $p \leq 0.01$, *** for $p \leq 0.001$, **** for $p \leq 0.0001$, and ns no significant difference. Graphic with relative signal intensities normalized to β-actin gene expression level. (A) Inflammatory gene fold expression (TNF-α, IL-1, IL-6, IL-12), where PCL–GL-6% Sc significantly downregulated IL-6 (*$p < 0.05$). (B) Apoptotic-related gene fold expression (P53, BAX, Bcl-2), with PCL–GL-6% Sc significantly upregulating Bax (****$p < 0.0001$) gene expression. (C) The genetic expression of angiogenesis genes (MMP-2, MMP-3, MMP-13), with PCL–GL-6% Sc significantly upregulating MMP-3 (**$p < 0.01$).

deposition and early-stage connective tissue formation. The presence of thin-walled capillaries suggests angiogenesis. However, the pale, lightly stained appearance of the ECM indicates a loose, disorganized structure, which may hinder cellular infiltration and tissue regeneration, contributing to a delayed wound-healing process.

In contrast, the PCL–GL-6% Sc treated group demonstrates significant histological improvements. H&E staining of the treated wound tissue reveals that this tissue is covered by a thick regenerated epithelium. The underlying dermis displays well-developed blood vessels and a stroma rich in fibroblasts. The presence of fine and coarse collagen strands indicates robust collagen formation, which supports tissue strength and integrity. Additionally, foci of calcification are observed, reflecting the effective maturation and stabilization of the newly formed tissue (Fig. 7V). Masson's trichrome stain of treated skin tissue (Fig. 7VI) displays regenerated keratinizing stratified squamous epithelium in red and fine strands of collagen in blue within the deeper dermal layers, suggesting enhanced collagen deposition and improved wound healing activity.

Immunohistochemistry (IHC) analysis was also conducted to visualize specific protein products within the tissue sections, thereby confirming the qPCR findings. Initially, vascular endothelial growth factor (VEGF), an essential player in the angiogenesis process, was detected. The results revealed moderate VEGF expression in the endothelial cells lining the blood vessels in both the negative control (Fig. 8A) and the PCL–GL-6% Sc-treated group (Fig. 8B). This cytoplasmic brownish staining, observed at 200× magnification, confirms that angiogenesis was actively occurring in both groups. In the negative control group, there was negative transforming growth factor

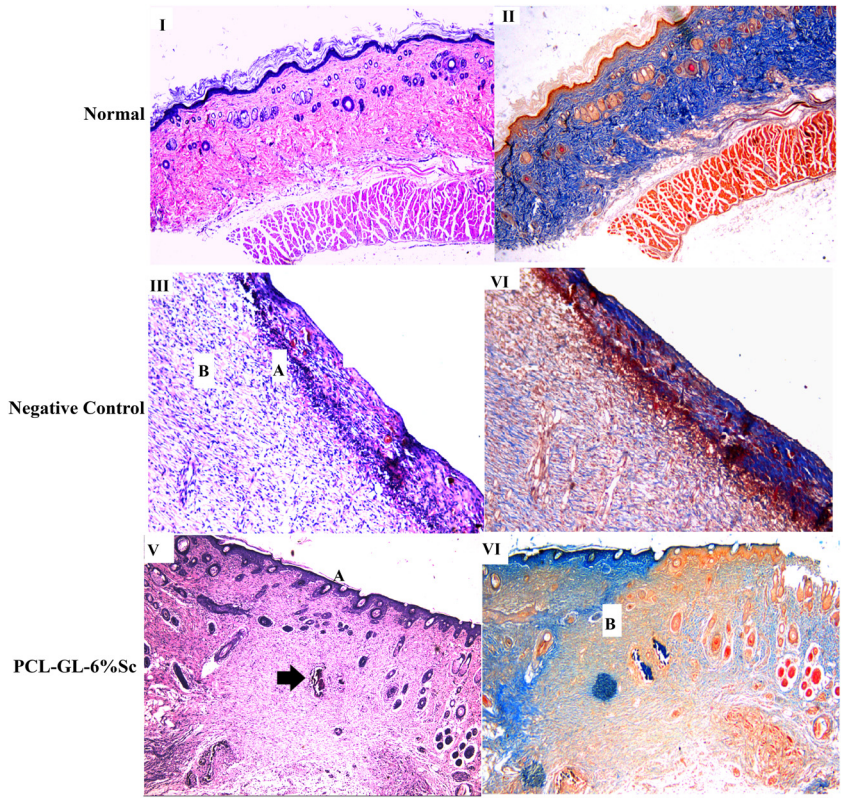

Fig. 7 Histological analysis of skin tissue and immune organs at magnification 100×. (I) and (II) Normal (uninjured) skin tissue stained with H&E and Masson's trichrome at, respectively. (III) and (IV) Negative control skin tissue stained with H&E (III), indicating a crust-covered wound with significant neutrophil infiltration (B), loosely organized ECM with minimal collagen fibers (A), and Masson's trichrome (IV) stain, showing early-stage connective tissue. (V) and (VI) PCL–GL-6% Sc treated skin tissue stained with H&E (V) reveals a thick regenerated epithelium (A), with foci of calcification indicating tissue maturation (Arrow), and Masson's trichrome (VI) stain, displaying enhanced collagen deposition (B).

β1 (TGF-β1) expression, with no significant staining observed (Fig. 8C). However, the PCL–GL-6% Sc treated group exhibited moderate TGF-β1 expression, with clear cytoplasmic brownish staining at 200× magnification (Fig. 8D). Results for BAX revealed negative expression in the negative control group, with no significant staining detected (Fig. 8E). In contrast,

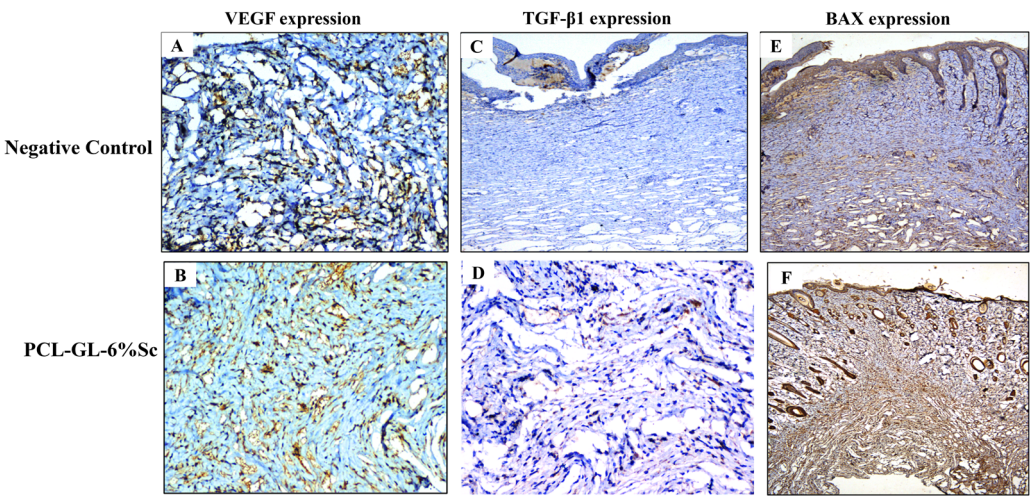

Fig. 8 Immunohistochemistry analysis of skin tissue. (A) and (B) Moderate VEGF expression in endothelial cells lining blood vessels is observed in both the negative control (A) and PCL–GL-6% Sc treated groups (B), with cytoplasmic brownish staining at 200× magnification. (C) and (D) TGF-β1 expression is negative in the negative control group (C) but shows moderate cytoplasmic brownish staining in the PCL–GL-6% Sc treated group (D) at 200× magnification. (E) and (F) BAX expression is negative in the control group (E), with strong cytoplasmic brownish staining in the PCL–GL-6% Sc treated group (F) at 40× magnification.

the PCL–GL-6% Sc treated group showed high BAX expression, as indicated by strong cytoplasmic brownish staining at 40× magnification (Fig. 8F), suggesting that the treatment may promote apoptosis in damaged cells.

4. Conclusions

This study demonstrates that PCL–GL nanofibers loaded with 6% *Saussurea costus* (Sc) extract significantly enhance wound healing compared to lower concentrations of Sc extract and untreated controls. Characterization of the nanofibers reveals an average diameter of 253.07 ± 44.54 nm for PCL–GL-6% Sc, with improved mechanical properties observed in tensile strength tests. Specifically, the PCL–GL-6% Sc nanofibers exhibited a Young's modulus of 4 ± 0.74 MPa, a yield strength of 0.409 ± 1.52 MPa, and an ultimate tensile strength of 0.563 ± 0.124 MPa. *In vitro* analyses show that PCL–GL-6% Sc nanofibers exhibited a cumulative Sc extract release of 54.6% over 7 days, which is higher than the amounts released from PCL–GL-2% Sc and PCL–GL-4% Sc (38.0% and 45.0%, respectively). Antimicrobial testing indicates a log reduction in bacterial colonies of *P. aeruginosa*, *S. aureus*, and *E. coli*, with the highest reduction achieved with PCL–GL-6% Sc. The DPPH scavenging activity of PCL–GL-6% Sc was 86.4%, significantly higher than that of PCL–GL and lower concentrations of Sc. Histological analysis reveals that PCL–GL-6% Sc treated wounds exhibit accelerated healing, with a 35% faster wound closure rate compared to the negative control group. The treatment significantly enhances collagen deposition, with Masson's trichrome stain showing increased collagen content. Immunohistochemistry confirms moderate VEGF expression and TGF-β1 expression in treated wounds, along with high BAX expression, indicating improved angiogenesis and apoptosis regulation. The PCR results show a significant upregulation of MMP-3 and BAX and a downregulation of IL-6 ($^{*}p < 0.05$). Furthermore, PCL–GL-6% Sc nanofibers were biocompatible and safe to the immune organs, with normal histological structures observed in the spleen and thymus. This study supports the potential of PCL–GL-6% Sc nanofibers as a highly effective and safe option for advanced wound healing applications. Further clinical studies and applications on wound healing are required to ensure efficacy and safety in humans.

Data availability

The data supporting this article have been included as part of the ESI.† Raw data is available upon request from the authors.

Conflicts of interest

The authors declare no conflict of interest in this work.

Acknowledgements

This work was supported by a DUP grant from the American University in Cairo to Distinguished University Professor Hassan M. E. Azzazy and a grant from the Science and Technology Development Fund (STDF; FLUG grant no. # 46721) to Professor Nagwa El-Badri.

References

1 A. A. Mamun, C. Shao, P. Geng, S. Wang and J. Xiao, *Front. Immunol.*, 2024, **15**, 1395479.
2 A. Uberoi, A. McCready-Vangi and E. A. Grice, *Nat. Rev. Microbiol.*, 2024, **22**, 507–521.
3 H. Guan, W. Dong, Y. Lu, M. Jiang, D. Zhang, Y. Aobuliaximu, J. Dong, Y. Niu, Y. Liu and B. Guan, *Front. Med.*, 2021, **8**, 609584.
4 K. Nuutila and E. Eriksson, *Adv. Wound Care*, 2021, **10**, 685–698.
5 C. Ersanli, A. Tzora, C. Voidarou, S. Skoufos, D. I. Zeugolis and I. Skoufos, *Biology*, 2023, **12**, 1187.
6 M. Mirhaj, S. Labbaf, M. Tavakoli and A. Seifalian, *Macromol. Biosci.*, 2022, **22**, 2200014.
7 A. E. B. Morguette, G. Bartolomeu-Gonçalves, G. M. Andriani, G. E. S. Bertoncini, I. M. D. Castro, L. F. D. A. Spoladori, A. M. S. Bertão, E. R. Tavares, L. M. Yamauchi and S. F. Yamada-Ogatta, *Plants*, 2023, **12**, 2147.
8 O. Yazarlu, M. Iranshahi, H. R. K. Kashani, S. Reshadat, S. Habtemariam, M. Iranshahy and M. Hasanpour, *Pharmacol. Res.*, 2021, **174**, 105841.
9 S. El-Ashram, L. M. El-Samad, A. A. Basha and A. El Wakil, *Pharmacol. Res.*, 2021, **170**, 105749.
10 A. Shafi, F. Hassan, I. Zahoor, U. Majeed and F. A. Khanday, in *Medicinal and Aromatic Plants: Healthcare and Industrial Applications*, ed. T. Aftab and K. R. Hakeem, Springer International Publishing, Cham, 2021, pp. 85–111, DOI: 10.1007/978-3-030-58975-2_3.
11 P. Kumari, S. Samant and S. Puri, *J. Med. Plants Stud.*, 2018, **6**, 45–68.
12 R. Kumari, M. Negi, P. Thakur, H. Mahajan, K. Raina, R. Sharma, R. Singh, V. Anand, L. C. Ming, K. W. Goh, D. Calina, J. Sharifi-Rad and A. Chaudhary, *Naunyn-Schmiedeb. Arch. Pharmacol.*, 2024, **397**, 1505–1524.
13 C. Benedetto, M. D'Auria, M. Mecca, P. Prasad, P. Singh, S. Singh, C. Sinisgalli and L. Milella, *Nat. Prod. Res.*, 2019, **33**, 2355–2358.
14 G. I. A. El-Rahman, A. Behairy, N. M. Elseddawy, G. E. Batiha, W. N. Hozzein, D. M. Khodeer and Y. M. Abd-Elhakim, *Antioxidants*, 2020, **9**, 1029.
15 N. Mammate, F. E. El Oumari, H. Imtara, S. Belchkar, A. Lahrichi, A. S. Alqahtani, O. M. Noman, M. Tarayrah and T. S. Houssaini, *Life*, 2022, **12**, 1026.
16 H. Idriss, B. Siddig, P. González-Maldonado, H. M. Elkhair, A. I. Alakhras, E. M. Abdallah, A. O. Elzupir and P. H. Sotelo, *Plants*, 2023, **12**, 460.
17 M. Azeez Akoul and M. Ghreeb, *Bionatura*, 2022, **7**(2), 33.
18 S. Alsharif, *Biosci. Res.*, 2022, 1607–1614.
19 L. A. Kolahalam, K. Prasad, P. M. Krishna and N. Supraja, *Heliyon*, 2021, **7**, e07265.

20 S. S. Hasson, M. S. Al-Balushi, J. Al-Busaidi, M. S. Othman, E. A. Said, O. Habal, T. A. Sallam, A. A. Aljabri and M. AhmedIdris, *Asian Pac. J. Trop. Biomed.*, 2013, **3**, 557–562.
21 M. Ashry, D. Gaber and K. Abdel-Wahhab, *Pak. J. Biol. Sci.*, 2021, **24**, 830–839.
22 H. Y. Ahmed, S. M. Kareem, A. Atef, N. A. Safwat, R. M. Shehata, M. Yosri, M. Youssef, M. M. Baakdah, R. Sami, R. S. Baty, N. H. Alsubhi, G. I. Alrefaei, A. A. Shati and F. G. Elsaid, *Antioxidants*, 2022, **11**, 1960.
23 T.-S. Yoon, Y.-Y. Sung, J.-Y. Jang, W.-K. Yang, Y.-U. Ji and H.-K. Kim, *Korean J. Med. Crop Sci.*, 2010, **18**, 151–156.
24 E. J. Chong, T. T. Phan, I. J. Lim, Y. Zhang, B. H. Bay, S. Ramakrishna and C. T. Lim, *Acta Biomater.*, 2007, **3**, 321–330.
25 X. Liu, H. Xu, M. Zhang and D.-G. Yu, *Membranes*, 2021, **11**, 770.
26 C. Gao, L. Zhang, J. Wang, M. Jin, Q. Tang, Z. Chen, Y. Cheng, R. Yang and G. Zhao, *J. Mater. Chem. B*, 2021, **9**, 3106–3130.
27 B. N. Blackstone, J. M. Hahn, K. L. McFarland, D. M. DeBruler, D. M. Supp and H. M. Powell, *Acta Biomater.*, 2018, **80**, 247–257.
28 N. Raina, R. Pahwa, J. K. Khosla, P. N. Gupta and M. Gupta, *Polym. Bull.*, 2022, **79**, 7041–7063.
29 A. Gaspar-Pintiliescu, A.-M. Stanciuc and O. Craciunescu, *Int. J. Biol. Macromol.*, 2019, **138**, 854–865.
30 J. Borges-Vilches, I. Unalan, K. Fernández and A. R. Boccaccini, *Polymers*, 2022, **14**, 2331.
31 M. Azizi, M. Azimzadeh, M. Afzali, M. Alafzadeh and S. H. Mirhosseini, *J. Adv. Mater. Process.*, 2018, **6**, 34–46.
32 M. M. Deabes, A.-E. Fatah, I. Sally, S. H. E. Salem and K. M. Naguib, *Egypt. J. Chem.*, 2021, **64**, 2833–2843.
33 K.-M. Chang and G.-H. Kim, *Prev. Nutr. Food Sci.*, 2008, **13**, 128–133.
34 J. Dulnik, P. Denis, P. Sajkiewicz, D. Kołbuk and E. Choińska, *Polym. Degrad. Stab.*, 2016, **130**, 10–21.
35 N. Reznikov, R. Almany-Magal, R. Shahar and S. Weiner, *Bone*, 2013, **52**, 676–683.
36 A. Dragich, M. McClendon, S. Hadi, A. C. Velez-Ortega and G. I. Frolenkov, 2024, DOI: **10.1093/mam/ozae044.479**.
37 K. Ren, Y. Wang, T. Sun, W. Yue and H. Zhang, *Mater. Sci. Eng., C*, 2017, **78**, 324–332.
38 M. P. Paarakh, P. A. Jose, C. Setty and G. Peterchristoper, *Int. J. Pharm. Res. Technol.*, 2018, **8**, 12–20.
39 S. Hatem, S. A. Elkheshen, A. O. Kamel, M. Nasr, N. H. Moftah, M. H. Ragai, R. S. Elezaby and N. M. El Hoffy, *Drug Delivery*, 2022, **29**, 1212–1231.
40 L. Marincas, N.-I. Farkas, L. Barbu-Tudoran, R. Barabas and M. I. Tosa, *Mater. Chem. Phys.*, 2023, **304**, 127862.
41 A. M. Moydeen, M. S. A. Padusha, E. F. Aboelfetoh, S. S. Al-Deyab and M. H. El-Newehy, *Int. J. Biol. Macromol.*, 2018, **116**, 1250–1259.
42 M. Esmaeilzadeh Kashi, V. Soheili, J. Asili, J. Davoodi, S. Soleimanpour, G. Karimi, S. F. Taghizadeh, R. Rezaee and A. Shakeri, *S. Afr. J. Bot.*, 2023, **154**, 260–264.
43 N. K. Mahdy, M. El-Sayed, S. E.-D. Al-Mofty, A. Mohamed, A. H. Karaly, M. E. El-Naggar, H. Nageh, W. A. Sarhan and H. M. El-Said Azzazy, *ACS Omega*, 2022, **7**, 38942–38956.
44 S. Lohrasbi, E. Mirzaei, A. Karimizade, S. Takallu and A. Rezaei, *Cellulose*, 2020, **27**, 927–940.
45 N. K. Sedky, Z. H. El Gammal, A. E. Wahba, E. Mosad, Z. Y. Waly, A. A. El-Fallal, R. K. Arafa and N. El-Badri, *J. Cell. Biochem.*, 2018, **119**, 3892–3902.
46 R. K. Nadda, A. Ali, R. C. Goyal, P. K. Khosla and R. Goyal, *J. Ethnopharmacol.*, 2020, **263**, 113199.
47 M. F. Soliman, Y. M. Shetaia, A. A. Tayel, A. M. Munshi, F. A. Alatawi, M. A. Alsieni and M. A. Al-Saman, *Antibiotics*, 2022, **11**, 327.
48 F. Yalcinkaya, B. Yalcinkaya and O. Jirsak, in *Electrospinning: Material, Techniques, and Biomedical Applications*, ed. S. A. H. Haider, IntechOpen, Rijeka Croatia, 2016, pp. 67–93.
49 K. F. Eidman and J. D. Belani, *e-EROS Encycl. Reagents Org. Synth.*, 2015, 1–7, DOI: **10.1002/047084289X.rf025.pub2**.
50 P. Denis, J. Dulnik and P. Sajkiewicz, *Int. J. Polym. Mater. Polym. Biomater.*, 2015, **64**, 354–364.
51 J. W. Kim, S. Park, K. Park and B.-K. Kim, *Appl. Sci.*, 2023, **13**, 1844.
52 G. El Fawal, H. Hong, X. Mo and H. Wang, *J. Drug Delivery Sci. Technol.*, 2021, **63**, 102501.
53 I. Unalan, S. J. Endlein, B. Slavik, A. Buettner, W. H. Goldmann, R. Detsch and A. R. Boccaccini, *Pharmaceutics*, 2019, **11**, 570.
54 E. A. Sander and V. H. Barocas, *J. Biomed. Mater. Res., Part A*, 2009, **88**, 322–331.
55 T. Clemons, M. Bradshaw, P. Toshniwal, N. Chaudhari, A. Stevenson, J. Lynch, M. Fear, F. Wood and K. S. Iyer, *RSC Adv.*, 2018, **8**, 9661–9669.
56 Y. Luo, N. Li, J. Tu, P. Shen, C. Huang, S. Lu and F. Zhang, Available at SSRN 5077609, DOI: **10.2139/ssrn.5077609**.
57 H. Xu, H. Li, Q. Ke and J. Chang, *ACS Appl. Mater. Interfaces*, 2015, **7**, 8706–8718.
58 F. A. Alshubaily, *Int. J. Biol. Macromol.*, 2019, **141**, 499–503.
59 V. T. Kimura, M. H. A. Zanin and S. H. Wang, *Polym. Bull.*, 2024, **81**, 9347–9361.
60 M. P. Das, P. Suguna, K. Prasad, J. Vijaylakshmi and M. Renuka, *Int. J. Pharm. Pharm. Sci.*, 2017, **9**, 239.
61 S. Gautam, C.-F. Chou, A. K. Dinda, P. D. Potdar and N. C. Mishra, *J. Mater. Sci.*, 2014, **49**, 1076–1089.
62 S. Gautam, C.-F. Chou, A. K. Dinda, P. D. Potdar and N. C. Mishra, *J. Mater. Sci.*, 2014, **49**, 1076–1089.
63 I. Rajzer, E. Menaszek, R. Kwiatkowski, J. A. Planell and O. Castano, *Mater. Sci. Eng., C*, 2014, **44**, 183–190.
64 D. Raj Preeth, S. Saravanan, M. Shairam, N. Selvakumar, I. Selestin Raja, A. Dhanasekaran, S. Vimalraj and S. Rajalakshmi, *Eur. J. Pharm. Sci.*, 2021, **160**, 105768.
65 S. Ravichandran, J. Radhakrishnan, P. Jayabal and G. D. Venkatasubbu, *Appl. Surf. Sci.*, 2019, **484**, 676–687.
66 M. Samy, B. Ekram, B. M. Abd El-Hady and M. M. Ayoub, *Polym. Bull.*, 2024, **81**, 3953–3972.
67 S. Gautam, A. K. Dinda and N. C. Mishra, *Mater. Sci. Eng., C*, 2013, **33**, 1228–1235.
68 P. Zadehnajar, K. Saeed, A. Babak and L. Ghasemi, *Mater. Technol.*, 2020, **35**, 39–49.
69 S.-C. Wong, A. Baji and S. Leng, *Polymer*, 2008, **49**, 4713–4722.

70 H. H. Kim, M. J. Kim, S. J. Ryu, C. S. Ki and Y. H. Park, *Fibers Polym.*, 2016, **17**, 1033–1042.
71 M. Adeli-Sardou, M. Torkzadeh-Mahani, M. M. Yaghoobi and M. Dodel, *Biomacromol. J.*, 2018, **4**, 46–57.
72 M. Dehghan, H. Nikukar and M. Khajeh Mehrizi, *Polym. Bull.*, 2022, **79**, 10881–10908.
73 M. Du, S. Liu, N. Lan, R. Liang, S. Liang, M. Lan, D. Feng, L. Zheng, Q. Wei and K. Ma, *Regen. Biomater.*, 2024, **11**, rbad114.
74 A. u R. Khan, M. Nadeem, M. A. Bhutto, F. Yu, X. Xie, H. El-Hamshary, A. El-Faham, U. A. Ibrahim and X. Mo, *Pharmaceutics*, 2019, **11**, 386.
75 A. Hivechi, P. B. Milan, K. Modabberi, M. Amoupour, K. Ebrahimzadeh, A. R. Gholipour, F. Sedighi, N. Amini, S. H. Bahrami, A. Rezapour, M. Hamidi and C. Delattre, *Polymers*, 2021, **13**, 854.
76 N. Palani, P. Vijayakumar, P. Monisha, S. Ayyadurai and S. Rajadesingu, *J. Nanobiotechnol.*, 2024, **22**, 211.
77 R. Szoleczky, A. Kovács, S. Berkó and M. Budai-Szűcs, *Pharmaceutics*, 2024, **16**, 313.
78 P. Patrojanasophon, S. Tidjarat, P. Opanasopit, T. Ngawhirunpat and T. Rojanarata, *Saudi Pharm. J.*, 2020, **28**, 1210–1216.
79 M. A. Barbosa, I. C. Gonçalves, P. M. D. Moreno, R. M. Gonçalves, S. G. Santos, A. P. Pêgo and I. F. Amaral, in *Comprehensive Biomaterials II*, ed. P. Ducheyne, Elsevier, Oxford, 2017, pp. 279–305, DOI: 10.1016/B978-0-12-803581-8.10246-2.
80 I. Sriyanti, D. Edikresnha, A. Rahma, M. M. Munir, H. Rachmawati and K. Khairurrijal, *Int. J. Nanomed.*, 2018, **13**, 4927–4941.
81 D. E. Estrella-Osuna, J. A. Tapia-Hernández, S. Ruíz-Cruz, E. Márquez-Ríos, J. D. J. Ornelas-Paz, C. L. Del-Toro-Sánchez, V. M. Ocaño-Higuera, F. Rodríguez-Félix, M. I. Estrada-Alvarado and L. A. Cira-Chávez, *Nanomaterials*, 2022, **12**, 2303.
82 M. Milosevic, D. B. Stojanovic, V. Simic, M. Grkovic, M. Bjelovic, P. S. Uskokovic and M. Kojic, *Sci. Rep.*, 2020, **10**, 11126.
83 Y. Fu and W. J. Kao, *Pharm. Res.*, 2009, **26**, 2115–2124.
84 E. Altun, E. Yuca, N. Ekren, D. M. Kalaskar, D. Ficai, G. Dolete, A. Ficai and O. Gunduz, *Pharmaceutics*, 2021, **13**, 613.
85 G. S. Ahmed and U. S. Coskun, *An. Acad. Bras. Cienc.*, 2023, **95**, e20230059.
86 R. E. Omer, F. H. M. Koua, I. M. Abdelhag and A. M. Ismail, *J. Appl. Pharm. Sci.*, 2019, **9**, 073–081.
87 R. M. O. Alaagib and S. M. H. Ayoub, *Pharma Innov.*, 2015, **4**, 73.
88 V. Duraipandiyan, N. Abdullah Al-Harbi, S. Ignacimuthu and C. Muthukumar, *BMC Complementary Altern. Med.*, 2012, **12**, 1–6.
89 K. Khorsandi, R. Hosseinzadeh, H. Esfahani, K. Zandsalimi, F. K. Shahidi and H. Abrahamse, *Inflamm. Regen.*, 2022, **42**, 40.
90 F. Nourbakhsh, M. Lotfalizadeh, M. Badpeyma, A. Shakeri and V. Soheili, *Phytother. Res.*, 2022, **36**, 33–52.
91 M. V. Ashraf, S. Pant, M. A. H. Khan, A. A. Shah, S. Siddiqui, M. Jeridi, H. W. S. Alhamdi and S. Ahmad, *Pharmaceuticals*, 2023, **16**, 881.
92 Q. Pang, Z. Jiang, K. Wu, R. Hou and Y. Zhu, *Antibiotics*, 2023, **12**, 351.
93 M. Fallah, S. H. Bahrami and M. Ranjbar-Mohammadi, *J. Ind. Text.*, 2016, **46**, 562–577.
94 H. M. Tag, H. E. Khaled, H. A. Ismail and N. S. El-Shenawy, *J. Basic Clin. Physiol. Pharmacol.*, 2016, **27**, 71–78.
95 M. Du, S. Liu, N. Lan, R. Liang, S. Liang, M. Lan, D. Feng, L. Zheng, Q. Wei and K. Ma, *Regen. Biomater.*, 2024, **11**, rbad114.
96 M. A. Shalaby, M. M. Anwar and H. Saeed, *J. Polym. Res.*, 2022, **29**, 91.
97 M. M. Lim and N. Sultana, *3 Biotechnol.*, 2016, **6**, 211.
98 M. M. Lim, T. Sun and N. Sultana, *J. Nanomater.*, 2015, **2015**, 303426.
99 P. Khazaeli, M. Alaei, M. Khaksarihadad and M. Ranjbar, *J. Nanobiotechnol.*, 2020, **18**, 176.
100 N. Yasrebi, A. H. Zarmi, M. Larypoor, M. Zeynali, B. Ebrahimi-Hosseinzadeh, Z. B. Mokhtari-Hosseini and H. Alvandi, *J. Polym. Res.*, 2021, **28**, 399.
101 N. Urao, J. Liu, K. Takahashi and G. Ganesh, *Adv. Wound Care.*, 2022, **11**, 598–621.
102 J. Wang, *Cell Tissue Res.*, 2018, **371**, 531–539.
103 L. Hong, P. Qiu, S. Niu, Q. Chen, X. Lu, F. Chen, M. Wen, N. Yu and Z. Chen, *Adv. Fiber Mater.*, 2024, **6**, 1993–1994.
104 K. Menclová, P. Svoboda, J. Hadač, Š. Juhás, J. Juhásová, J. Pejchal, V. Mandys, K. Eminger and M. Ryska, *Mil. Med.*, 2021, **188**, e133–e139.
105 B. Z. Johnson, A. W. Stevenson, C. M. Prêle, M. W. Fear and F. M. Wood, *Biomedicines*, 2020, **8**, 101.
106 P. Schilrreff and U. Alexiev, *Int. J. Mol. Sci.*, 2022, **23**, 4928.
107 X. Yang, J. Zeng, X. Yu, Z. Wang, D. Wang, Q. Zhou, T. Bai and Y. Xu, *Ann. Clin. Microbiol. Antimicrob.*, 2023, **22**, 103.
108 T. T. Nguyen, S. Mobashery and M. Chang, *Wound healing-new insights into ancient challenges*, 2016, vol. 10.